bioRxiv preprint doi: https://doi.org/10.1101/573279; this version posted March 16, 2019. The copyright holder for this preprint (which was not certified by peer review) is the author/funder, who has granted bioRxiv a license to display the preprint in perpetuity. It is made available under aCC-BY-NC-ND 4.0 International license.

Transcriptomic and Cellular Decoding of Regional Brain Vulnerability to Neurodevelopmental Disorders

Jakob Seidlitz[a,b,*], Ajay Nadig[a], Siyuan Liu[a], Richard A.I. Bethlehem[b], Petra E. Vértes[b,c,d], Sarah E. Morgan[b], František Váša[b], Rafael Romero-Garcia[b], François M. Lalonde[a], Liv S. Clasen[a], Jonathan D. Blumenthal[a], Casey Paquola[e], Boris Bernhardt[e], Konrad Wagstyl[b,f], Damon Polioudakis[g], Luis de la Torre-Ubieta[g,h], Daniel H. Geschwind[g,i], Joan C. Han[j,k,l], Nancy R. Lee[m], Declan G. Murphy[n], Edward T. Bullmore[b,o,p], and Armin Raznahan[a,*]

[a]Developmental Neurogenomics Unit, National Institute of Mental Health, Bethesda, MD, USA.
[b]University of Cambridge, Department of Psychiatry, Cambridge, UK.
[c]School of Mathematical Sciences, Queen Mary University of London, London, UK.
[d]The Alan Turing Institute, London, UK.
[e]McConnell Brain Imaging Centre, Montreal Neurological Institute and Hospital, Montreal, QC, Canada.
[f]McGill Centre for Integrative Neuroscience, McGill University, Montreal, QC, Canada.
[g]Department of Neurology, Center for Autism Research and Treatment, Semel Institute, David Geffen School of Medicine, UCLA, Los Angeles, CA, USA.
[h]Department of Psychiatry and Biobehavioral Sciences, Semel Institute, David Geffen School of Medicine, UCLA, USA.
[i]Department of Human Genetics, David Geffen School of Medicine, UCLA, Los Angeles, CA, USA.
[j]Departments of Pediatrics and Physiology, University of Tennessee Health Science Center and Le Bonheur Children's Foundation Research Institute, Memphis, TN, USA.
[k]Pediatrics and Developmental Neuropsychiatry Branch, National Institute of Mental Health, NIH, Bethesda, MD, USA.
[l]Unit on Metabolism and Neuroendocrinology, *Eunice Kennedy Shriver* National Institute of Child Health and Human Development, NIH, Bethesda, MD, USA.
[m]Drexel University, Department of Psychology, Philadelphia, PA, USA.
[n]King's College London, Institute of Psychiatry, London, UK.
[o]Cambridgeshire and Peterborough NHS Foundation Trust, Huntingdon, UK.
[p]GlaxoSmithKline R&D, Stevenage, UK.
* Correspondence to jakob.seidlitz@nih.gov or raznahana@mail.nih.gov

bioRxiv preprint doi: https://doi.org/10.1101/573279; this version posted March 16, 2019. The copyright holder for this preprint (which was not certified by peer review) is the author/funder, who has granted bioRxiv a license to display the preprint in perpetuity. It is made available under aCC-BY-NC-ND 4.0 International license.

Neurodevelopmental disorders are a major public health concern but remain poorly understood in biological terms. In particular, although we know that genetically-distinct neurodevelopmental disorders induce distinct changes in regional brain anatomy, we do not understand how such specificity arises. Here, by leveraging diverse neurodevelopmental disorders of known genetic origin, we show that this specificity can be explained by cell-type dependent gradients of gene expression that are evident in the healthy brain. We first used in vivo structural neuroimaging to map altered cortical organization in neurodevelopmental disorders arising due to 6 different genomic copy number variation (CNV) disorders, including both duplications (chromosomes X, Y and 21) and deletions (X-chromosome, 22q11.2, 11p13). Comparisons with publicly-available postmortem gene expression maps from healthy adults revealed that the spatial pattern of anatomical change in each disorder was preferentially associated with the spatial expression profile for genes within the causal CNV region. Next, by gathering a comprehensive set of single-cell gene expression signatures, and using normative postmortem data to map expression gradients for each canonical cell class in the brain, we identified specific cell-classes that expressed CNV genes and closely tracked the spatial pattern of cortical disruption in each disorder (e.g. *NCAM2*-expressing oligodendrocyte precursors in Down syndrome, *MAPK1*-expressing inhibitory neurons in del22q11.2, *PTCHD1*-expressing astrocytes in X-chromosome aneuploidies). Finally, we used two orthogonal approaches to validate our imaging-transcriptomic associations against direct measures of altered gene expression in tissue from CNV carriers. First, we demonstrated that CNV genes with differential dosage sensitivity in patients show patterns of brain expression that were differentially correlated with cortical disruption. Second, we established that CNV patients with more severely disrupted gene expression in blood-derived tissue show more extreme cortical disruption in brain MRI. Thus, cell-type dependent gradients of gene expression that are intrinsic to the human brain can be used to infer disease-specific drivers of regional brain vulnerability without reference to any postmortem brain tissue in patients. Furthermore, this "transcriptional vulnerability model" for prediction of regional neuroanatomical disruption makes it possible to estimate the severity of altered brain organization in a given patient from the severity of altered gene expression in their blood.

Neurodevelopmental disorders are associated with spatially selective changes in brain structure and function[1–3], but we currently lack an understanding of how such specificity arises. Addressing this gap in knowledge would identify mechanisms for regional brain vulnerability in patients, with important consequences for translational neuroscience. There is emerging evidence that intrinsic spatial gradients of gene expression within the brain may partly explain regional brain vulnerability to developmental and degenerative disorders in humans[4–7]. However, to date, definitive tests of this "*transcriptional vulnerability model*" have only been conducted in mice, where causal genetics lesions can be experimentally defined a priori[8,9]. We currently lack similarly definitive "gene-first" tests of the transcriptional vulnerability model in humans, or an understanding of which specific aspects of brain organization could "translate" pathogenic alterations of specific gene sets into spatially-distributed disruptions of brain anatomy.

bioRxiv preprint doi: https://doi.org/10.1101/573279; this version posted March 16, 2019. The copyright holder for this preprint (which was not certified by peer review) is the author/funder, who has granted bioRxiv a license to display the preprint in perpetuity. It is made available under aCC-BY-NC-ND 4.0 International license.

The current study provides a series of strict, independent tests of the transcriptional vulnerability model in humans by assembling a large body of existing structural neuroimaging data from diverse genetically-defined neurodevelopmental disorders arising due to known chromosomal or sub-chromosomal copy number variations (CNVs). By linking these neuroimaging data to publicly-available maps of gene expression in the human brain, we are able to ask if the observed neuroanatomical changes in each disorder are preferentially correlated with expression patterns of the defining causal genes for that disorder. We further validate our observations against independent surveys of cell-specific gene expression in the human brain, and direct measures of altered gene expression in patients.

Our study included a total of 518 structural magnetic resonance imaging (sMRI) brain scans from matched case-control cohorts spanning 8 different neurogenetic disorders: XXX, XXY, XYY, XXYY, trisomy 21 (Down syndrome), X-monosomy (Turner syndrome), del22q11.2 (velocardiofacial syndrome, VCFS) and del11p13 (Wilms Tumor-Aniridia syndrome, WAGR) (**Table S1**; Total N = 231 patients, 287 controls). These scans were used to map changes in cortical anatomy for each of 6 different CNV conditions: +X, +Y, +21, -X, -22q11, -11p13 (**Methods**). Cortical changes were characterized using morphometric similarity (MS) mapping – a MRI marker of brain structure based on a combination of features typically studied such as cortical thickness, surface area, curvature[10]. We have previously shown that cortical MS gradients are closely-aligned with cortical cytoarchitecture, connectivity, and gene expression[10]. In this study, we calculated person level MS maps, and used these to compute a MS change map for each CNV condition relative to matched controls (**Fig. 1a, Fig. S1, Methods**).

Each of the 6 CNVs studied induced a distinct spatial pattern of MS change across the cortex, with regionally-specific MS increases (red) and decreases (blue) relative to healthy control participants (**Fig. 1b**). Supplementary analyses (i) confirmed that the distinctiveness of MS change in each CNV was not an artifact of differences between the cohorts of healthy individuals against which each CNV was being compared (**Fig. S2a**), and (ii) detailed the distinct patterns of anatomical disruption which underlay regional MS increases vs. decreases in patients relative to controls (**Methods, Fig. S2b)**. Having defined the spatial pattern of MS change in each disorder, we next asked if these MS change maps were preferentially correlated with intrinsic brain expression patterns for the gene sets that defined each disorder.

Each CNV's anatomical change map was aligned to the same publicly-available atlas of gene expression for ~15k genes in adult human cortex from the Allen Human Brain Atlas (AHBA dataset)[11] (**Methods, Fig. 1a, Fig. S1**). We used partial least squares (PLS) regression to rank all ~15k genes in this atlas by their multivariate correlation[12,13] with each CNV MS change map – resulting in one ranked gene list for each disorder (**Fig. 1a, Extended Data Table 1**). In these lists, genes with expression patterns that are more strongly correlated with the disease-related MS change map from MRI have large positive or negative PLS weights and therefore occupy more extreme ranks. The polarity of these ranked lists was set so that genes with strongly positive PLS weights had positive spatial correlations between their expression with MS change in patients vs. controls, and occupied extreme low ranks (i.e., closer to c. -7500, **Fig. 1a**). Conversely, genes with strongly negative PLS weights were expressed in spatial patterns that correlated negatively with MS change in patients vs. controls and occupied extreme high ranks (i.e., closer to c. +7500, **Fig. 1a**). These ranked gene lists therefore provided a quantitative framework for testing the transcriptional vulnerability model (**Fig. 1a**). Specifically, for each

bioRxiv preprint doi: https://doi.org/10.1101/573279; this version posted March 16, 2019. The copyright holder for this preprint (which was not certified by peer review) is the author/funder, who has granted bioRxiv a license to display the preprint in perpetuity. It is made available under aCC-BY-NC-ND 4.0 International license.

disorder, we assessed if the median rank for genes in the CNV region was more extreme than would be expected by chance. This prediction was confirmed for all 6 CNVs (**Fig. 1b, Table S2**).

In all 3 CNVs involving an abnormal gain of genetic material (+X, +Y, +21), the relevant chromosomal gene set showed a higher median rank than all other chromosomal gene sets (**Fig. 1b**). Conversely, in all 3 CNVs involving an abnormal loss of genetic material, genes within the CNV region occupied relatively low median ranks (**Fig. 1b;** versus all other chromosomes for -X, and versus random cis gene sets of matched size for -22q11.2 and -11p13). Thus, for these 6 different genetically-defined neurodevelopmental disorders, brain regions showing relatively high expression of the causal gene set in health tended to show MS decreases in patients carrying a duplication of the gene set, and MS increases in patients carrying a deletion of that gene set. Conversely, brain regions showing relatively low expression of the causal gene set in health tended to show MS increases in patients with gene set deletion, and MS increases in gene set duplication. For all 6 CNVs studied, except +Y, the the above median rank results were statistically significant at $P < 0.05$ relative to at least one of 3 different null gene rank models: i) 10000 gene rank permutations (P_{RAND} or $P_{RAND\text{-}Chr}$), ii) gene ranks from 10000 spatial rotations of the original anatomical change map (P_{SPIN}), and iii) gene ranks from anatomical differences in 10000 bootstrap resamples of patient/control labels (P_{BOOT}) (**Fig. 1a, Table S2, Methods**). Supplementary analyses clarified that the weaker statistical significance of these tests for the +Y CNV condition was a predictable consequence of the small number of Y-linked genes with available brain expression data (**Fig. S3a**). Repeating the above analyses using anatomical change maps for individual MS features (e.g. cortical thickness, surface area, etc.), indicated that MS change maps performed better than individual features for recovering the specific relationships between cortical gene expression and anatomical change in each CNV (**Fig. S3b, Table S3**). The CNV-specific gene rankings generated by our integration of neuroimaging and transcriptomic data (**Extended Data Table 1**) could not only be validated against prior knowledge of the genes within each CNV (**Fig. 1**, **Table S2**) but also against independent gene ontology (GO) annotations. Rank-based GO term enrichment analyses identified “biological process” (BP) and “cellular component” (CC) annotations that were overrepresented amongst genes with extreme PLS loadings (e.g., for -22q11.2, extreme high ranking genes: ion transport (BP) and axon (CC), extreme low ranking genes: cell signaling (BP) and plasma membrane (CC), **Extended Data Table 2**).

Given that regional differences in cortical gene expression are thought to largely reflect regional differences in cellular composition of the cortex[14], we reasoned that the spatial correspondence between expression of CNV genes in health and anatomical changes in CNV carriers (**Fig. 1**) could arise through the combination of (i) a spatially-patterned representation of different cell types across the cortex, and (ii) a patterned expression of CNV genes across cell types. In order to test these linked hypotheses, we compiled 57 independent cell-specific gene sets from 5 independent large-scale single-cell studies of the adult human cortex (**Methods, Extended Data Table 3**). To first verify that the mature cortex shows systematic regional differences in its expression of cell-specific gene sets, we used the AHBA dataset to calculate maps for the median expression of each cellular gene set across the cortex (**Methods**). Unsupervised hierarchical clustering of this cell-by-region expression matrix using the gap-statistic criterion[15] distinguished three broad cell groups with distinct patterns of regional expression (**Fig. 2b**): (i) oligodendrocytes, (ii) other glial and endothelial cells, and (ii) excitatory

bioRxiv preprint doi: https://doi.org/10.1101/573279; this version posted March 16, 2019. The copyright holder for this preprint (which was not certified by peer review) is the author/funder, who has granted bioRxiv a license to display the preprint in perpetuity. It is made available under aCC-BY-NC-ND 4.0 International license.

and inhibitory neurons. Further co-clustering of cells within these three groups by the similarity in their regional expression profiles (**Fig. 2b, Methods**) recovered seven canonical cell classes within the central nervous system: microglia, endothelial cells, oligodendrocyte precursors (OPCs), oligodendrocytes, astrocytes, excitatory and inhibitory neurons. We derived a single omnibus gene set for each of these seven cell classes by collapsing across study-specific gene sets, and we then visualized the mean expression for each cell class gene set across the cortex (**Fig. 2b, Methods**). These transcriptomic proxy maps for cellular patterning across the human cortex could be validated against several independently-generated maps of cortical microstructure from neuroimaging and histology (**Methods, Fig. S4**). For example (i) expression gradients for the oligodendrocyte cell class showed a statistically significant ($P_{SPIN} < 0.05$) positive coupling with maps of intracortical myelination as indexed by in vivo magnetization transfer imaging[12], whereas (ii) expression gradients for astrocytes showed significantly positive spatial coupling with several histological and neuroimaging markers for associative cortices with expanded supragranular layer thickness[16–18] ($P_{SPIN} < 0.05$).

Having defined and validated these cell class-specific gradients of cortical gene expression in health, we next tested for association between the regional expression of these cell classes and the observed MS changes in each CNV disorder (**Methods**). Specifically, for each CNV, we identified cell classes which met the following two independent criteria. First, the gene set for that cell class had to possess a significantly extreme median rank ($P_{RAND} < 0.05$) in the ranked gene list for that CNV (**Extended Data Table 1,** from the aforementioned PLS analyses), indicating significant spatial coupling between expression of the cell signature and MS change in the CNV. Second, the gene set for that cell class had to include one or more genes from within the CNV region that had an extreme median rank (i.e., top/bottom 5% PLS ranks). The pairing of these criteria results in a highly conservative filter given that the primary single cell gene expression studies used in our analyses focused on genes that were uniquely or highly expressed in a given cell. Nevertheless, this filter powerful insights into potential CNV disease mechanisms by identifying specific CNV genes that were expressed in specific cell classes that showed strong expression signatures in specific foci of anatomical vulnerability to the relevant CNV (**Fig. 2b**). For example, we established that MS increases in Down syndrome patients relative to controls are positively coupled to the expression gradient of oligodendrocyte precursor cells which express the chromosome 21 gene *NCAM2* as part of their cell-specific expression signature. Strikingly, this gene and this cell type have each been independently implicated in the neurobiology of Down syndrome by prior research in model systems and patient postmortem brain tissue[19,20], but not yet integrated and linked to large-scale brain changes in the disorder. Similarly novel gene-cell-region motifs were discovered for all other CNVs examined (except +Y), including: *PAX6*-expressing astrocytes in cortical regions of MS-increase in -11p13 (WAGR) syndrome; *MAPK1*-expressing inhibitory neurons in regions of MS-increase in -22q11.2 (VCFS) syndrome; and a close spatial coupling between MS change in X-chromosome CNVs and expression gradients of oligodendrocytes, endothelial cells and astrocytes (which express neurodevelopmentally-pertinent X-linked genes including *AMMECR1, ITM2A* and *PTCHD1*, respectively). Importantly, our analytic approach yielded these highly specific and falsifiable hypotheses regarding cell-specific drivers of regions of altered brain development in each CNV without reference to any postmortem brain tissue from patients, but

bioRxiv preprint doi: https://doi.org/10.1101/573279; this version posted March 16, 2019. The copyright holder for this preprint (which was not certified by peer review) is the author/funder, who has granted bioRxiv a license to display the preprint in perpetuity. It is made available under aCC-BY-NC-ND 4.0 International license.

based solely on more readily acquired clinical neuroimaging data combined with publicly-available maps of gene expression in the human brain.

Given the "genetics-first" nature of our study design, the above findings provide quasi-experimental evidence in humans that the spatial patterning of neurodevelopmental disorders on regional brain anatomy is organized by intrinsic brain expression patterns of disease-relevant genes. Having demonstrated that this transcriptional vulnerability model applies in humans, we next sought to provide the first validations of this model against direct measures of altered gene expression in patients. Specifically, we tested for evidence in support of two independent predictions from the transcriptional vulnerability model: (i) the spatial coupling between CNV-induced anatomical changes and brain gene expression should differ between CNV genes that show robust expression changes in patients (i.e. dosage sensitive, DS), and those that do not (nDS), and (ii) amongst carriers of a given CNV, individuals who show a greater changes in DS gene expression should also show more pronounced anatomical changes along the spatial expression gradient for DS genes. We tested both these hypotheses using transcriptomic data from CNV carriers[21–23].

To test the first of these hypotheses, we used recently-published gene expression studies in patients with +21, +X, and -X CNVs[21–23] to define DS and nDS gene sets for each CNV (**Methods, Fig. 3b, Extended Data Table 4**). Data were available from brain tissue in +21, and from blood-derived lymphoblastoid cell lines (LCLs) in +21, +X and -X, yielding 4 paired DS and nDS gene sets. For each CNV, we then tested if these DS and nDS gene sets differed in their spatial correlation with observed cortical anatomy changes (by comparing gene set median ranks in the relevant PLS-derived ranked gene list from **Extended Data Table 1**). This prediction was confirmed for all 3 CNVs, ($P_{RAND} < 0.05$, **Fig. 3b**), and held for DS/nDS sets defined in blood-derived LCLs as well as brain tissue. The fact that genes with differing dosage sensitivity in patient LCLs also showed differing spatial coupling between expression and regional anatomical changes in the brain suggests that cis-effects of a CNV on gene expression may be reproducible across tissue types. This notion is supported by prior research in model systems[24], and our own observation of a statistically-significant correlation across genes between the magnitude of expression change for chromosome 21 genes in brain tissue vs. in LCLs from patients with Down syndrome ($r = 0.34$, $P_{RAND} = 0.04$, **Methods**).

For all 3 CNVs considered, median rank differences between DS and nDS gene sets were driven by a small subset of DS genes (DS^{SS}, **Fig. 3b,** rank decile analysis**, Methods**). For +21 and +X, DS^{SS} genes possessed strongly positive PLS weights, indicating that they are most highly-expressed in cortical regions of MS increase in patients vs. controls (e.g., +21: insula and cingulate cortex, +X: precuneus, lateral temporal lobe), and least expressed in regions of MS reduction (e.g., +21: fronto-parietal areas, +X: anterior cingulate). Conversely, for -X, DS^{SS} genes possessed strongly negative PLS weights, indicating that they are most highly-expressed in cortical regions of MS decrease in patients vs. controls and least expressed in regions of MS increase. Thus, for all 3 CNV conditions considered, the spatial patterning of cortical MS changes was preferentially correlated with the patterned expression of CNV genes, but in opposite directions for DS^{SS} vs. nDS gene sets (i.e., **Fig. 1b** vs. **Fig. 3b**, respectively). These observations indicated that the relative expression of DS^{SS} vs. nDS genes could provide a strong predictor of regional cortical MS change in these neurodevelopmental disorders. This inference was verified for all three disorders ($P_{SPIN} < 0.001$, **Fig. 3c**).

bioRxiv preprint doi: https://doi.org/10.1101/573279; this version posted March 16, 2019. The copyright holder for this preprint (which was not certified by peer review) is the author/funder, who has granted bioRxiv a license to display the preprint in perpetuity. It is made available under aCC-BY-NC-ND 4.0 International license.

To test our second hypothesis – that severity of altered gene expression amongst patients would predict severity of cortical anatomy change – we used a subset of patients with abnormal sex chromosome dosage who had provided blood sample for gene expression analysis in addition to sMRI brain scans (N=55, karyotypes: XXX, XXY, XXYY). As part of a prior study, these blood samples had been used to make LCLs, from which we had measured expression for 11 DS X-chromosome genes by qPCR[21] (**Methods**). Regional MS maps were calculated for all these patients from their sMRI data as described above and detailed in **Methods**. To interrelate peripheral gene expression and cortical MS across individuals we (i) scaled regional MS and gene expression within each karyotype group (to remove potential between-karyotype effects), (ii) used PLS regression to define the principal component of shared variance between gene expression and MS, and (iii) compared the variance explained and cortical patterning of this component relative to null distributions provided by 10000 permutations breaking the linkage between participant scans and qPCR data (i.e., P_{BOOT}, **Methods**). The observed principal component was statistically-significant ($P_{BOOT} = 0.0094$) and had cortical region loadings which closely recapitulated the spatial gradient of MS change in individuals carrying an extra X chromosome ($P_{SPIN} < 0.0001$, **Methods, Fig. 4b**). Thus, CNV-induced changes in cortical anatomy are not only coupled to regional variation in the cortical expression of CNV genes in health (**Fig. 1**), but also to inter-individual variation in the expression of genes that show dosage sensitivity to that CNV as measured in blood-derived LCLs (**Fig. 4**).

The methods and results presented above offer several new theoretical and empirical inroads into the biology of neurodevelopmental disorders. First, by studying genetically-defined (rather than behaviorally-defined) patient cohorts, we provide quasi-experimental evidence in humans that intrinsic expression gradients of disease-defining genes organize the spatial targeting of altered brain development in neurodevelopmental disorders (**Fig. 1**). Second, we demonstrate that these intrinsic gene expression gradients can themselves be grounded in the patterned expression of genes across different cell types, and the patterned expression of cell-types across the brain. Thus, cellular organization of the human brain provides a framework for translating disease-related alterations of specific genes into disease-related alterations of specific distributed brain regions. We exploit this cellular framework to generate novel and highly-articulated hypotheses about the specific genes and cell-types that are most likely to underpin regional cortical disruptions in patients with Down, VCFS, WAGR and sex chromosome aneuploidy syndromes (**Fig. 2**). Such data-driven footholds can accelerate biological research into neurodevelopmental disorders by allowing a new level of precision in the targeting of future mechanistic studies (**Extended Data Table 1**). Critically, we generate these disorder-specific results through on an unbiased analytic approach that screens many potential brain regions, cell classes and genes without relying on postmortem tissue from patients or generalization from model systems. This provides a practical advantage given the scarcity of postmortem brain tissue from patients (especially those with rare genetic disorders), and also enables us to make predictions regarding the biology of distinctly human disorders using data from native human tissue. Third, for full CNVs of chromosomes X and 21, we were able to refine the transcriptional vulnerability model by integrating data from prior studies of gene expression in CNV carriers. These analyses indicated that the spatial patterning of altered cortical anatomy in carriers of these whole chromosome CNVs is most closely related to

bioRxiv preprint doi: https://doi.org/10.1101/573279; this version posted March 16, 2019. The copyright holder for this preprint (which was not certified by peer review) is the author/funder, who has granted bioRxiv a license to display the preprint in perpetuity. It is made available under aCC-BY-NC-ND 4.0 International license.

regional differences in the balance between expression of two chromosomal gene sets within the human brain: those that show significant changes in expression with changes in chromosome dosage and those that do not (**Fig. 3**). This observation for full-chromosomal CNVs may generalize to other classes of genetic risks for neurodevelopmental disorders, such that regional transcriptional vulnerability is determined by a multivariate interaction between (i) the patterned impact of a genetic variants across multiple genes, and (ii) the patterned expression of these genes in a given brain regions relative to other brain regions. Finally, for full CNVs of the X-chromosome, we use paired measures of brain anatomy and gene expression within the same patient cohort to show that the cortical change map induced by carriage of an extra X-chromosome is more pronounced in patients who show more altered expression of dosage sensitive X-chromosome genes in blood-derived LCLs (**Fig. 4**). This finding uses the axis of inter-individual variation to provide orthogonal validation of the transcriptional vulnerability model, and also points towards the potential of using measures of gene expression in blood-derived tissue to predict the severity of brain phenotypes in CNV carriers. We speculate this this predictive relationship arises because inter-individual variation amongst CNV carriers for the expression levels of CNV genes is partially correlated across tissues. This hypothesis is consistent with observation that the proximal effects of a CNV on expression of genes within the CNV region are relatively stable across tissues[24], and will be amenable to direct empirical analysis when there are large datasets of multi-tissue expression across multiple individuals carrying the same CNV.

In summary, our study adopts a genetic-first approach to provide the first quasi-experimental support in humans that the spatial patterning of neurodevelopmental disorders on regional brain anatomy is organized by intrinsic brain expression patterns of disease-relevant genes. We further show that this “transcriptional vulnerability model” for prediction of regional vulnerability can be linked to cell-type dependent patterning of gene expression, and validated against direct measures of gene expression in patients. The methods and results we present provide new biological insights into several of the specific neurogenetic disorders studied, as well as a novel generalizable framework for transcriptomic and cellular decoding of brain disorders from in vivo neuroimaging data. Crucially, despite not requiring access to any postmortem brain tissue from patients, or inference from model systems, the methods we present can screen the large multidimensional search space of brain regions, cell types, and genes to propose highly-specific mechanistic targets for developmental disorders of the human brain.

bioRxiv preprint doi: https://doi.org/10.1101/573279; this version posted March 16, 2019. The copyright holder for this preprint (which was not certified by peer review) is the author/funder, who has granted bioRxiv a license to display the preprint in perpetuity. It is made available under aCC-BY-NC-ND 4.0 International license.

Methods

Cohorts, Diagnostic Classification, and MRI Acquisition

National Institutes of Health - Bethesda, USA (NIH)

Sex Chromosome Aneuploidies: This dataset has been described in detail previously[25–27]. Briefly, we included 297 patients with various supernumerary X- and/or Y-chromosome counts and 165 healthy controls (79 females) (**Table S1**). Patients were recruited through the National Institutes of Health (NIH) website and parent support groups. X- and Y-supernumeracy was confirmed by karyotype testing. Exclusion criteria included a history of head injury, neurological condition resulting in gross brain abnormalities, and mosaicism (determined by visualization of 50 metaphase spreads in peripheral blood). Healthy controls were enrolled in longitudinal studies of typical brain development[28]. Exclusion criteria for controls included the use of psychiatric medication, enrollment in special education services, history of mental health treatment, or prior diagnosis of a medical condition that impacts the nervous system. Full-scale IQ was measured with the WASI. Subjects were scanned on a 1.5T GE Signa scanner (axial slices = 124 x 1.5 mm, TE = 5 ms, TR = 24 ms, flip angle = 45°, acquisition matrix = 256 x 192, FOV = 24 cm) using a spoiled-gradient recalled echo (3D-SPGR) imaging sequence. The research protocol was approved by the institutional review board at the National Institute of Mental Health, and informed consent or assent was obtained from all individuals who participated in the study, as well as consent from their parents if the child was under the legal age of majority.

Down Syndrome / Trisomy 21: This dataset has been described in detail previously[2]. Briefly, we included 26 patients (13 females) with Down Syndrome and 42 healthy controls (21 females) (**Table S1**). All participants with DS had a chromosomal diagnosis of Trisomy 21 according to parent report or direct testing, with no instances of mosaicism. In addition to the genetic inclusion criteria, participants were also required be free of any history of acquired head injury or other condition that would cause gross brain abnormalities. Full-scale IQ was measured as follows: for participants under the age of 18, the Differential Ability Scales, Second Edition[29] was administered, and for participants 18 and older, the Kaufman Brief Intelligence Test, Second Edition[30] was administered. Imaging was completed without sedation on the same 3-Tesla General Electric Scanner using an 8-channel head coil. High-resolution (0.94 x 0.94 x 1.2 mm) T1-weighted images were acquired utilizing an ASSET-calibrated magnetization prepared rapid gradient echo sequence (128 slices; 224 x 224 acquisition matrix; flip angle = 12°; field of view [FOV] = 240 mm). The research protocol was approved by the institutional review board at the National Institute of Mental Health, and informed consent or assent was obtained from all individuals who participated in the study, as well as consent from their parents if the child was under the legal age of majority.

Wilms Tumour-Aniridia Syndrome (WAGR): A total of 31 patients with heterozygous contiguous gene deletions of incremental variable length on the short arm of chromosome 11 (11p13 deletion), and 23 healthy controls participated in a comprehensive genotype/phenotype study approved by the NIH IRB and with the informed consent of their parents/legal guardians.

bioRxiv preprint doi: https://doi.org/10.1101/573279; this version posted March 16, 2019. The copyright holder for this preprint (which was not certified by peer review) is the author/funder, who has granted bioRxiv a license to display the preprint in perpetuity. It is made available under aCC-BY-NC-ND 4.0 International license.

Healthy controls were screened and excluded for history of neurological and psychological impairments. Chromosome deletions were characterized by microsatellite marker analysis and oligonucleotide array comparative genomic hybridization. Neuropsychological assessments were conducted using standardized psychological tests. All participants underwent MRI structural brain imaging. Imaging quality controls included visual inspection of the raw images for motion artifacts as well as the quality of the surface and volume segmentations. The image processing results were inspected for surface and volume segmentation errors by FML and AR. The MRI brain scans were collected at one cubic millimeter resolution using a 3D TFE T1-weighted sequence on a 3.0 T Philips Achieva MRI scanner equipped with an 8-channel phased array head coil. The sequence parameters were as follows: TR = 8.3 ms, TE = 3.8 ms, TI delay = 1031 ms, 160 shots. In total, 171 slices were acquired in the sagittal plane with an acquisition matrix of 240 by 240 and an FOV of 240 millimeters. Ethical approval was obtained from the local Ethics Committee. All participants (or their legal guardians) gave informed consent.

Institute of Psychiatry - London, UK (IoP)

Turner Syndrome (X-monosomy): This cohort and associated data have been described in depth previously[31,32]. We included 20 females with X-monosomic Turner's Syndrome (TS) and 36 healthy controls in this study (**Table S1**). Briefly, participants with TS were recruited through a university-based behavioral genetics research program run in collaboration with the South London and Maudsley NHS Foundation Trust and typically developing controls through local advertisement. Karyotype was determined for each participant with TS by analyzing thirty metaphase spreads using conventional cytogenetic techniques. No participants suffered from any psychiatric or medical disorders that would grossly affect brain function (e.g. epilepsy, neurosurgery, head injury, hypertension, schizophrenia) as determined by structured clinical interview and examination, as well as review of medical notes. Structural MRI data were acquired using a GE Signa 1.5T Neuro-optimised MR system (General Electric, Milwaukee, Wisconsin). Whole head coronal 3D-SPGR images (TR = 14 ms, TE = 3 ms, 256 x 192 acquisition matrix, 124 x 1.5 mm slices) were obtained from all subjects. Ethical approval was obtained from the local Ethics Committee and informed written consent was obtained from all participants.

Velocardiofacial Syndrome VCFS): This dataset has been used and described in depth previously[33,34]. Briefly, all patients with VCFS and control subjects were screened for medical conditions affecting brain function by means of a semi-structured clinical interview and routine blood tests. Full-scale intelligence was measured by means of the Canavan et al shortened version of the Wechsler Adult Intelligence Scale–Revised[35]. We included 27 controls (11 females) alongside 29 participants (13 females) with clinical features of VCFS (**Table S1**) and a 22q11.2 deletion detected by fluorescence *in situ* hybridization (FISH; Oncor Inc, Gaithersburg, MD, USA). Subjects were scanned on a 1.5T GE Signa scanner at the Maudsley Hospital in London, UK. A whole-head 3D-SPGR image was acquired for each subject (TR = 11.9 ms; TE = 5.2 ms; 256 x 192 acquisition matrix; 124 x 1.5 mm slices). Ethical approval was obtained from the local Ethics Committee. All subjects (or their guardians, when subjects < 16 years old) gave written informed consent after the procedure was fully explained.

bioRxiv preprint doi: https://doi.org/10.1101/573279; this version posted March 16, 2019. The copyright holder for this preprint (which was not certified by peer review) is the author/funder, who has granted bioRxiv a license to display the preprint in perpetuity. It is made available under aCC-BY-NC-ND 4.0 International license.

Image Processing and Generation of Morphometric Similarity Networks

All T1-weighted (T1w) scans were processed using the Montreal Neurological Institute's CIVET pipeline[36] (v1.1.10). Due to the lack of multimodal imaging, only (gray matter) morphometric features derived from the T1-weighted scans were estimated (CT: cortical thickness, SA: surface area, GM: gray matter volume, MC: mean curvature, IC: intrinsic curvature). GM values were estimated using the T1w volumes of each subject. Vertex-wise CT and SA values were estimated using the resultant pial surface reconstructions from CIVET, while MC and IC metrics of these surfaces were estimated using the freely available Caret5 software package[37]. These surface meshes (~80,000 vertices per mesh) were downsampled into our regional parcellation (below), where the vertex-wise estimates of the features were averaged within a given region in the parcellation. Cortical surface representations were plotted using BrainsForPublication v0.2.1 (https://doi.org/10.5281/zenodo.1069156).

For each subject, regional morphometric features (CT, SA, GM, MC, and IC) were first scaled (Z-scored, per feature across regions) to account for variation in value distributions between the features. After normalization, Morphometric Similarity Networks (MSNs) were generated by computing the regional pairwise Pearson correlations in morphometric feature sets, yielding an association matrix representing the strength of morphometric similarity between each pair of cortical areas[10]. For all individuals, regional MS estimates were calculated as the average morphometric similarity for between a given cortical region and all others.

Cortical Parcellation

We generated a 308-region (n=152 LH regions) cortical parcellation using a back-tracking algorithm to restrict the parcel size to be approximately 500mm^2, with the Desikan-Killiany atlas boundaries as starting points[38,39] This parcellation has been used in previous structural[12,40,41] and functional[13] imaging studies of connectomes, and was also used in our first study of MSNs[10].

Statistical Analyses of MSN Differences

For each cohort, group-wise effects of disease on nodal similarity were modeled using the 'glm' base function in R, with sex and age included as covariates. This model was fitted for each region, and the two-sided T-statistic (contrast = patient - control) was extracted (represented in **Fig. 2a** as a Z-score for plotting purposes). For the SCA groups, we collectively modeled each chromosome dosage effect as follows:

$$NS_i \sim intercept + \beta 1(age) + \beta 2(sex) + \beta 3(Xan) + \beta 4(Yan), \quad (1)$$

bioRxiv preprint doi: https://doi.org/10.1101/573279; this version posted March 16, 2019. The copyright holder for this preprint (which was not certified by peer review) is the author/funder, who has granted bioRxiv a license to display the preprint in perpetuity. It is made available under aCC-BY-NC-ND 4.0 International license.

Where NS_i is the nodal similarity estimate across subjects at region *i*, and Xan and Yan are the number of supernumerary X and Y chromosomes (respectively). This was done after ruling out any significant interactions between Xan and sex, or Xan and Yan for variation in nodal similarity[1].

For the +21, -X, -22q11.2, -11p13 patient-control comparisons in nodal similarity (NS_i), the following model was used:

$$NS_i \sim intercept + \beta 1(age) + \beta 2(sex) + \beta 3(Dx), \quad (2)$$

Where Dx is the binary classification of patients and controls.

These procedures resulted in MS change maps for 6 different CNV conditions, which were taken into subsequent analyses (+X, +Y, +21, -X, -22q11, -11p13).

Interpretation of Regional Morphometric Similarity Differences

Due to the zero-centered nature of the regional morphometric similarity (MS) distribution (**Fig. S2a**), we annotated the regional MS change maps (T-statistics) to determine the underlying effects at the edge level (i.e., "connections"). For each CNV, we first computed the edgewise MS change between patients and controls (i.e., Eqs 1 or 2 for each edge, or pairwise correlation). Then, for the top 10 positive (red in **Fig. 1b**) and 10 negative (blue in **Fig. 1b**) regional MS T-statistics we took the absolute sum of their corresponding edge T-values for each of four possible types of edge effect:

- "hypercoupling" = an edge with a positive weight in controls, and a positive edge T-statistic for the CNV effect (i.e. regions which are morphometrically similar in controls being rendered more similar by the CNV)

- "dedifferentiation" = an edge with a negative weight in controls, and a positive edge T-statistic for the CNV effect (i.e. regions which are morphometrically dissimilar in controls being rendered less dissimilar by the CNV)

- "decoupling" = an edge with a positive weight in controls, and a negative edge T-statistic for the CNV effect (i.e. regions which are morphometrically similar in controls being rendered less similar by the CNV)

- "hyperdifferentiation" = an edge with a negative weight in controls, and a negative edge T-statistic for the CNV effect (i.e. regions which are morphometrically dissimilar in controls being rendered more dissimilar by the CNV)

These four effects are depicted in the legend of **Fig. S2b**.

bioRxiv preprint doi: https://doi.org/10.1101/573279; this version posted March 16, 2019. The copyright holder for this preprint (which was not certified by peer review) is the author/funder, who has granted bioRxiv a license to display the preprint in perpetuity. It is made available under aCC-BY-NC-ND 4.0 International license.

Derivation of Gene Sets for each CNV

Assignments of AHBA genes to chromosome locations were made according to those from Richiardi et al. (2015)[42]. These assignments defined the gene sets used for all chromosome-level analyses. Gene sets for the two sub-chromosomal CNVs in our study were defined as follows. The 11p13-deletion (WAGR) gene set was defined using the known distribution of proximal and distal breakpoints in the WAGR patient cohort studied (relative to the NCB136/hg18 genome assembly, references via the USCS Genome Browser). We used the median proximal and distal breakpoints across patients to define a representative chromosomal segment for use in analysis, which encompassed 45 AHBA genes in total (**Extended Data Table 1**) including both WAGR critical region genes (WT1 and PAX6). As patient-specific breakpoint data were not available for the 22q11.2-deletion (VCFS) cohort, we defined the gene set for this CNV using reference breakpoints for the most common A-D deletion type (seen in >85% of patients)[43], which encompassed 20 genes from the AHBA dataset.

Transcriptomic Alignment of Neuroimaging Data

Methods for the alignment of the microarray gene expression data from 6 adult human donors, provided by the Allen Human Brain Atlas (AHBA), to the left hemisphere (n = 152 regions) of our parcellation has been described in depth elsewhere[4,10,40], where we have shown that the gene expression data is robust to leaving a given donor out of the analysis. Briefly, we used FreeSurfer's *recon-all* to reconstruct and parcellate the cerebral cortex of each AHBA donor using the corresponding T1-weighted volume[44]. Tissue samples were assigned to the nearest parcel centroid of the left hemisphere of our parcellation in each subject's native space. For the two subjects with right hemisphere data, we first reflected the right hemisphere samples' coordinates and then performed the mapping. The median regional expression was estimated for each gene across participants (N = 6) and then each gene's regional values were normalized (Z-scored), resulting in a 152 (regions) × 15043 (genes) matrix of the genome-wide expression data for the left hemisphere. The code and data underlying the AHBA alignment is available online at https://github.com/RafaelRomeroGarcia/geneExpression_Repository.

Partial Least Squares Regression of MS Differences

This method – applied in similar analyses integrating neuroimaging and brain gene expression data – has been described previously[4,12] (see also **Fig. S1**). Here, we employ PLS regression to rank AHBA genes by their multivariate spatial alignment with cortical MS changes in each of 6 different CNV conditions (+X, +Y, +21, -X, -22q11, -11p13). As detailed below, these ranked gene list for each CNV condition (**Extended Data Table 1**) provide a unifying framework to test for preferential spatial alignment between CNV-induced MS change and the spatial expression user-defined gene sets of interest (e.g. genes within vs. without the CNV region, gene sets defining different cell types etc.).

bioRxiv preprint doi: https://doi.org/10.1101/573279; this version posted March 16, 2019. The copyright holder for this preprint (which was not certified by peer review) is the author/funder, who has granted bioRxiv a license to display the preprint in perpetuity. It is made available under aCC-BY-NC-ND 4.0 International license.

Briefly, partial least squares (PLS) regression is a data reduction technique closely related to principal component analysis (PCA) and ordinary least squares (OLS) regression. Here we use the SIMPLS algorithm[45] in R ('pls' package[46]), where the independent variable matrix (X) and the dependent variable (Y) is centered giving rise to X_0 and Y_0 respectively. The first component is then weighted by w_1 and q_1 to calculate factor scores (or PLS component scores) T_1 and U_1.

This T_1 is the weighted sum of the centered independent variable:

$$T_1 = X_0 w_1 + E_1, \quad (4)$$

And U_1 is the weighted sum of the centered dependent variable:

$$U_1 = Y_0 q_1 + E_2, \quad (5)$$

The weights and the factors scores are calculated to ensure the maximum covariance between T_1 and U_1, which is a departure from regular PCA where the scores and loadings are calculated to explain the maximum variance in X_0.

The SIMPLS algorithm provides an alternative where the matrices are not deflated by the weights when calculating the new components, and, as a result, it is easier to interpret the components based on the original centered matrices.

As the components are calculated to explain the maximum covariance between the dependent and independent variable, the first component need not explain the maximum variance in the dependent variable. However, as the number of components calculated increases, they progressively tend to explain less variance in the dependent variable. We verified that the first component (U_1, used for gene rank analysis) for each CNV-specific PLS explained the most relative variance.

For each CNV, we used U_1 to rank genes by their PLS loadings (from large positive to large negative PLS loadings, **Fig. 1a**). The polarity of the PLS components was fixed so that gene ranks would have the same meaning across all CNVs. Thus, for all CNV-induced MS change maps, genes with large positive PLS weights had higher than average expression in cortical regions where MS is increased in CNV carriers relative to controls (i.e., red regions in **Fig. 1b**), and lower than average expression in cortical regions where MS is decreased in CNV carriers relative to controls (i.e., blue regions in **Fig. 1b**). Conversely, genes with large negative PLS weights had higher than average expression in cortical regions where MS is reduced in CNV carriers relative to controls (i.e. blue regions in **Fig. 1b**), and lower than average expression in cortical regions where MS is increased in CNV carriers relative to controls (i.e. red regions in **Fig. 1b**). Mid-ranking genes with smaller PLS weights showed expression gradients that are weakly related to the pattern of cortical MS change.

It is important to note that T_1 and U_1 are the first PLS component weights in the common dimension of the X and Y variables. Thus, in our analyses comparing AHBA gene expression to

bioRxiv preprint doi: https://doi.org/10.1101/573279; this version posted March 16, 2019. The copyright holder for this preprint (which was not certified by peer review) is the author/funder, who has granted bioRxiv a license to display the preprint in perpetuity. It is made available under aCC-BY-NC-ND 4.0 International license.

cortical MS change (as in the example interpretation above), the common dimension is at the level of the nodes. However, in our analyses comparing individual patient gene expression to individual cortical MS maps, the common dimension was people rather than brain regions (see below).

Median Rank Gene Enrichment Analysis

The ranked gene lists provided by PLS regression of AHBA expression and MS change provided a common framework to test if the spatial expression of a given gene set was non-randomly related to an observed spatial pattern of MS change. Specifically, we quantified this degree of spatial correspondence or a given gene set using used an objective and simple measure of median gene set rank. This allowed for interpretation of "rank enrichment" both relative to the center of the rank distribution, and relative to the extremes of the list. One primary, and two secondary nulls were used to compare the observed median ranks compared to those expected by chance. The primary null distribution for significance testing was generated by 10000 gene rank permutations (P_{RAND}). We also compared observed gene set ranks against two orthogonal nulls distributions: gene ranks from 10000 spatial rotations of the relevant MS change map (P_{SPIN}), and gene ranks from anatomical differences in 10000 bootstrap resamples of patient/control labels (P_{BOOT}).

For the full chromosome CNVs, median ranks were assessed for chromosomes 1:22, X, Y, and the pseudoautosomal region (PAR, or "X|Y"). For plotting purposes, results with full chromosomes are presented in **Fig. 1b**, and results with all chromosomes and PAR genes are shown in **Table S2**. For the sub-chromosomal deletions (-22q11.2/VCFS and -11p13/WAGR), we performed an additional variant of our P_{RAND} test ($P_{RAND\text{-}Chr}$), only comparing observed median ranks to those for 10000 from gene sets of equivalent size resampled from relevant chromosome (i.e., chromosome 22 for -22q11.2 and chromosome 11 for -11p13).

Given that CNV gene sets varied greatly in size, and the smallest gene set (+Y), was notable for being the only gene set that had an observed median ran that fell below the nominal P_{RAND} = 0.05 threshold, we conducted supplementary analyses to investigate the relationship between CNV gene set size and the statistical significance of observed CNV gene set median ranks relative to the P_{RAND} null distribution. We decided to nest these analyses in the context of the X-chromosome, which was the CNV that contained the greatest number of linked genes in the AHBA. Across evenly-spaced subsamples of the X-chromosome gene set, ranging from the set size of the Y-chromosome (smallest whole-chromosome CNV) to the full size of the X-chromosome, we generated 10000 median gene ranks from the +X PLS-ranked gene list within each subsample, as well as median gene ranks from random pulls of the entire (AHBA-overlapping) genome of comparable set size (**Fig. S3a**). Since pairs of X-chromosome subsets and random subsets were arbitrarily matched, subsample P-values were calculated by testing the median of the X-chromosome median gene ranks against the 10000 null median gene ranks generated by the random pulls. This was performed for each subsample size (**Fig. S3a**) to evaluate a "predicted" P-value for median ranks of CNV gene sets sized similarly to the CNVs

bioRxiv preprint doi: https://doi.org/10.1101/573279; this version posted March 16, 2019. The copyright holder for this preprint (which was not certified by peer review) is the author/funder, who has granted bioRxiv a license to display the preprint in perpetuity. It is made available under aCC-BY-NC-ND 4.0 International license.

(+Y, +21) observed in our study.

Due to the fact that MS change maps integrated information from multiple individual anatomical metrics (e.g. cortical thickness, surface area, etc.), we tested if anatomical change maps for each of these individual MS features were also capable of recovering the preferential relationship between CNV effects on cortical anatomy and corotical expression gradients for CNV genes. To achieve this, we repeated the analytic steps detailed above for each CNV, replacing the MS change map with change maps for every individual metric used as part of our 5-feature MS mapping (**Fig. S3b**): gray matter volume, cortical thickness, surface area, mean curvature and intrinsic curvature. PLS-derived gene ranks from all these analyses were assessed for statistically-significant extreme ranking of CNV gene sets ($P_{RAND} < 0.05$, **Table S3**).

Gene Ontology Enrichment Analyses

Functional enrichment was assessed using rank-based gene ontology (GO) enrichment analysis. First, we subsetted the full PLS-ranked gene lists for each CNV to only contain genes that were determined as brain-expressed (see below). Then, each refined "brain-only" CNV gene list was inputted to GOrilla[47,48] ordered by PLS score separately in increasing and decreasing order to obtain enrichments for both tails of the gene list. Full output can be found in **Extended Data Table 2**.

Collation and Anatomical Projection of Single Cell Gene Expression Data

We compiled data from 5 different single-cell studies using postmortem cortical samples in human postnatal subjects[49–53], to avoid any bias based on acquisition methodology or analysis or thresholding.

To obtain gene sets for each cell type, categorical determinations were based on each individual study, as per the respective methods and analysis choices in the original paper. All cell-type gene sets were available as part of the respective papers. For the Zhang et al. (2016) and Darmanis et al. (2015) papers, these data had already been reported elsewhere[54], and therefore were re-used in the present study. This approach to led to the initial inclusion of 58 cell classes, many of which were overlapping based on nomenclature and/or constituent genes. The genes within each of these 58 cell-types are compiled in **Extended Data Table 3**.

We generated spatial maps of expression for each cell type gene set by calculating the median regional expression score for each gene set in the AHBA bulk microarray dataset (**Fig. 2a**). Then we performed hierarchical clustering of this region-by-cell-type expression matrix, using the gap statistic[15] criterion. This unsupervised analysis enabled us to determine if the cell type gene sets from diverse studies could be grouped into biologically-grounded clusters by their patterned expression across the cortical sheet. The clustering of study-specific gene sets according to known cell classes was taken to indicate that gene expression gradients in the

bioRxiv preprint doi: https://doi.org/10.1101/573279; this version posted March 16, 2019. The copyright holder for this preprint (which was not certified by peer review) is the author/funder, who has granted bioRxiv a license to display the preprint in perpetuity. It is made available under aCC-BY-NC-ND 4.0 International license.

cortical sheet are partly organized by cell-type.

Data-driven Recovery of Canonical Cell Classes based on Expression Topographies

The convergence of cell-type expression topography allowed us to cluster individual study cell-type gene lists into canonical cell classes. Within the context of the N=3 hierarchical clustering solution from **Fig. 2a** we performed post-hoc assignment of each study-specific cell-type into a cell classes based on visualization of the t-Distributed Stochastic Neighborhood Embedding (tSNE) solution (**Fig. 2b**) on the data from **Fig. 2.** This solution clearly organized study-specific cell types into 7 canonical classes, which were fully nested within the N=3 hierarchical clustering solution from **Fig. 2a**. These 7 classes were: Astrocytes (Astro), Endothelial cells (Endo), Microglia (Micro), Excitatory Neurons (Neuro-Ex), Inhibitory Neurons (Neuro-In), Oligodendrocytes (Oligo), and Oligodendrocyte Precursor Cells (OPC).

To derive expression maps for each of these 7 cell classes, we first collapsed across study-specific gene lists to generate a single omnibus gene list for each cell class, and then calculated a weighted average expression for each cell class gene set in each region of our 152 AHBA parcellation (**Fig. 2c**). Weights for each underlying cell-type were computed by estimating the Euclidean distance of each cell-type from the centroid of their respective cell class using principal component analysis. Two studies did not subset neurons into excitatory and inhibitory, and thus these gene sets were excluded from this cell class assignment. Additionally, only one study included the annotation of the “Per” (pericyte) type, and thus this gene set was also excluded.

Cortical Map Comparison of Overall Cell Class Expression

To validate the individual cell class expression maps derived from integration of single cell expression studies and AHBA microarray data (**Fig. 2c**), we computed the spatial correlation of each cell class expression map to established maps of cortical microstructure from diverse in vivo neuroimaging and postmortem histological studies, including maps of cytoarchitecture[55] myeloarchitecture[12], and gradients of evolutionary[17], developmental[17], and inter-individual (allometric) anatomical scaling[16] (**Fig. S4**).

For the cytoarchitectonic maps, a 100µm resolution volumetric histological reconstruction of a post mortem human brain from a 65-year-old male was obtained from the open-access BigBrain[55] repository on February 2, 2018 (https://bigbrain.loris.ca/main.php). Using previously defined surfaces of the layer 1/11 boundary, layer 4 and white matter[18], we divided the cortical mantle in supragranular (layer 1/11 to layer 4) and infragranular bands (layer 4 to white matter). Band thickness was calculated as the Euclidean distance between the respective surfaces. To approximate cellular density, we extended upon recent work on BigBrain microstructure profiles[56] and generated microstructure profiles within supra- and infra-granular bands. Intensity profiles using five equivolumetric surfaces within the predefined surfaces of the BigBrain were

bioRxiv preprint doi: https://doi.org/10.1101/573279; this version posted March 16, 2019. The copyright holder for this preprint (which was not certified by peer review) is the author/funder, who has granted bioRxiv a license to display the preprint in perpetuity. It is made available under aCC-BY-NC-ND 4.0 International license.

then averaged to produce an approximate density value. Calculations were performed at 163,842 matched vertices per hemisphere, then averaged within each cortical region in our parcellation.

Methods for generation of comparison myeloarchitecture and anatomical scaling maps used in these analyses have been detailed previously[12,16,17,55].

Spatial Permutation Testing of Correspondence Between Cell-Class Expression and Other Cortical Maps

To assess specificity of the correspondence between pairs of cortical maps, we generated 10000 "spins" of the cortical parcellation[10,41]. This matching provides a mapping from the set of regions to itself, and allows any regional measure to be permuted while controlling for spatial contiguity and hemispheric symmetry.

We first obtained the spherical surface coordinates of each of our 308 regions on the fsaverage template in Freesurfer. These were then rotated about the three principal axes at three randomly generated angles. Given the separate left- and right-hemisphere cortical projections, the rotation was applied to both hemispheres. However, to preserve symmetry, the same random angles were applied to both hemispheres with the caveat that the sign of the angles was flipped for the rotations around the y and z axes.

Following each rotation, coordinates of the rotated regions were matched to coordinates of the initial regions using Euclidean distance, proceeding in a descending order of average Euclidean distance between pairs of regions on the rotated and unrotated spheres (i.e., starting with the rotated region that is furthest away, on average, from the unrotated regions).

Relating Cell-Class Gene Expression Gradients to CNV-induced MS Changes

Our analysis of expression gradients for previously reported single cell expression signatures (see above) yielded a omnibus gene set for each of seven canonical cell classes. We assessed the relationship between cortical expression of these cell classes and cortical MS change in each CNV by considering two complementary features. First, we identified cell class gene sets that occupied significantly extreme ranks in each CNV's ranked gene list from AHBA ($P_{RAND} < 0.05$). This rank-based criterion provides a test for the degree of spatial coupling between cortical expression of each cell class and each CNV change map. Then, amongst the cell classes that met this rank-based criterion for a given CNV, we examined the expression of CNV genes to identify cells clases that expressed CNV genes which (i) were independently recorded as being brain expressed from proteomic data (see below), and (ii) were occupied extreme ranks (<5th, or >95th centile) alongside the cell class gene list in the relevant CNVs ranked gene list.

bioRxiv preprint doi: https://doi.org/10.1101/573279; this version posted March 16, 2019. The copyright holder for this preprint (which was not certified by peer review) is the author/funder, who has granted bioRxiv a license to display the preprint in perpetuity. It is made available under aCC-BY-NC-ND 4.0 International license.

Defining Dosage Sensitive Genes in Down Syndrome (+21) and X-chromosome Aneuploidies.

Dosage sensitive (DS) genes were defined as those within the CNV region that were reported to show a statistically-significant fold change in congruence with the genomic copy number change (i.e., increased in duplication carriers vs. controls or decreased in deletion carriers vs. controls).

Prior reports enabled us to define DS genes in +21 for two different tissue types: brain[22] and blood-derived lymphoblastoid cell lines (LCLs)[23]. Brain DS genes were defined as all chromosome 21 genes determined to show developmentally-stable and statistically significant upregulation in patient vs. controls by authors of a prior study of postmortem brain tissue (see Table S3 from [22]). The LCL DS gene set was defined as all chromosome 21 genes found to be significantly up-regulated in LCLs from postnatal +21 CNV carriers relative to controls (see Table 3 from [23]). For each tissue, non-dosage sensitive (nDS) chromosome 21 genes were defined as those within the AHBA dataset that did not fall within the respective tissue DS set.

For X-chromosome aneuploidies, DS X-linked genes were defined using a prior microarray study[21] of X-chromosome dosage effects on gene expression in LCLs from participants with a wide range of X-chromosome complements. X-linked LCL DS genes were defined as all X-linked genes with expression levels showing a significant positive association with X-chromosome count variation across a wide karyotype range spanning X-chromosome monosomy (i.e., -X CNV), euploidy, and X-chromosome duplication states (i.e., +X CNV). This criterion (see Supplementary Information Text S3 from [21]) defined 40 DS genes for -X and +X CNVs. Non-dosage sensitive genes for these CNV conditions were defined as all X-linked genes within the AHBA dataset that did not fall within the DS gene set.

We used median rank comparisons to test if DS and nDS genes showed patterns of cortical expression that were differentially correlated to cortical MS changes in each CNV (**Fig. 3b** left). Specifically, the observed difference between median ranks of DS and nDS sets was compared to the differences of 10000 gene rank permutations (P_{RAND}).

Decile Score Analysis for Dosage Sensitive Genes

A median rank difference between two gene sets could be driven by a difference in overall rank distribution between gene sets, or by a subgroup of genes in one or both sets with extreme ranks. We used rank decile analysis to differentiate these two scenarios. Specifically, we (i) computed the difference in the proportion of genes in the DS vs. nDS gene sets for each decile of the CNV ranked gene lists, and (ii) tested for deciles with significant differences at $P_{RAND} < 0.05$ (see **Fig. 3b** right). For all four instances of DS-nDS gene set comparison (+21 brain-derived sets ; +21, -X, +X LCL-derived sets), median rank differences between the DS and nDS gene set were driven by a small subset of extreme-ranked DS genes (DS^{SS}, **Figs. 3b,c, Extended Data Table 4**).

bioRxiv preprint doi: https://doi.org/10.1101/573279; this version posted March 16, 2019. The copyright holder for this preprint (which was not certified by peer review) is the author/funder, who has granted bioRxiv a license to display the preprint in perpetuity. It is made available under aCC-BY-NC-ND 4.0 International license.

For all three CNVs considered in these analyses (+21, +X, -X) the median rank for these DS^{SS} CNV genes was of an opposite polarity to that observed for the CNV gene set as a whole (c.f. **Fig. 3c**, **Fig. 1b**). This observation implied that observed cortical MS changes in +21, +X and -X CNVs could be relating to two opposing cortical gradients of CNV gene expression: those for DS^{SS} genes vs. those for nDS genes. To verify this inference, we compared the cortical pattern of MS change for each of these CNVs from neuroimaging data, to the cortical pattern of differential expression for DS^{SS} vs. nDS gene sets as calculated from AHBA postmortem data (**Fig. 3d**).

Linking Peripheral Gene Expression and Brain Anatomy in X-chromosome Aneuploidies

These analyses sought to validate the relationship between CNV gene expression and cortical MS using the axis of interindividual variation. We could test the relationship between inter-individual variation of gene expression and cortical MS using a subset of 55 CNV carriers in our study from whom we had gathered measures of LCL gene expression as well as sMRI brain scans. These study participants all carried an extra X-chromosome (11 XXX, 23 XXY, 11 XXYY), and originated from the National Institutes of Health Sex Chromosome Aneuploidy cohort. Details of sMRI data collection and MS map calculation for this cohort have already been described above. As part of a previously-published gene expression study, we had also generated qRT-PCR (quantitative reverse transcription polymerase chain reaction) measures of gene expression in LCL tissue from these participants for 11 DS X-linked genes. These 11 genes had been selected based on a genome-wide microarray screen for X-chromosome dosage effects on LCL gene expression in sex chromosome aneuploidy conditions[21]. The methods for generation, pre-processing and analysis of these qRT-PCR data have been detailed previously[21]. Briefly, RNA was extracted by standard methods (Qiagen), and qRT-PCR was performed using the Fluidigm platform. For data processing, an assay with Ct > 23 was deemed to be not expressed. Expression data were normalized relative to the averaged expression of the two housekeeping genes ACTB and B2M, which were not differentially expressed across groups in either microarray or rtPCR data.

Before inter-relating gene expression and cortical MS across these 55 +X carriers, we first scaled gene expression and MS data across individuals within each karyotype group to remove between-karyotype group effects. This enabled us to test if, within any given +X karyotype group, greater disruption of DS gene expression was related to a cortical MS map that more strongly resembled the +X MS change map (**Fig. 1b**). To achieve this test we used PLS regression to interrelate interindividual variation in gene expression and interindividual variation in cortical MS (see above). Partial Least Squares regression defined a principal component of covariance between gene expression and cortical MS across patients, and feature loadings onto this component: one for each gene, and one for each cortical region. The cortical region loadings from this PLS component were then compared to the +X cortical MS change map in order to test of those regions which are most sensitive to X chromosome dosage are also those that vary most with interindividual variation in expression of DS X-linked genes amongst carriers of an extra X chromosome. This map comparison consisted of computing the spatial correlation

bioRxiv preprint doi: https://doi.org/10.1101/573279; this version posted March 16, 2019. The copyright holder for this preprint (which was not certified by peer review) is the author/funder, who has granted bioRxiv a license to display the preprint in perpetuity. It is made available under aCC-BY-NC-ND 4.0 International license.

between PLS loadings and the +X MS change map, and comparing this correlation to the distribution of 10000 correlations given by random spatial rotations of the +X MS change map (i.e., P_{SPIN}).

Defining Brain-Specific Genes

For the gene ontology (GO) enrichment analyses and the single-cell enrichment analyses detailed below, we first thresholded our "whole-genome" gene set (N=15043) to only contain genes that were determined as brain-expressed via the Human Protein Atlas (https://www.proteinatlas.org/) database of normal tissue expression. Genes whose levels of expression were "not-detected" in the cerebral cortex were excluded, yielding a list of N=7971 genes with detected brain expression (**Extended Data Table 5**).

Data Availability

Relevant code and processed data for generating the findings and figures presented in this manuscript will be made available on Github, and the brain maps will be made available on Neurovault (all links to be provided at time of publication).

bioRxiv preprint doi: https://doi.org/10.1101/573279; this version posted March 16, 2019. The copyright holder for this preprint (which was not certified by peer review) is the author/funder, who has granted bioRxiv a license to display the preprint in perpetuity. It is made available under aCC-BY-NC-ND 4.0 International license.

References

1. Raznahan, A. *et al.* Globally Divergent but Locally Convergent X- and Y-Chromosome Influences on Cortical Development. *Cereb. Cortex* **26**, 70–79 (2016).
2. Lee, N. R. *et al.* Dissociations in Cortical Morphometry in Youth with Down Syndrome: Evidence for Reduced Surface Area but Increased Thickness. *Cereb. Cortex* **26**, 2982–2990 (2016).
3. Schmitt, J. E. *et al.* Aberrant Cortical Morphometry in the 22q11.2 Deletion Syndrome. *Biol. Psychiatry* **78**, 135–143 (2015).
4. Romero-Garcia, R., Warrier, V., Bullmore, E. T., Baron-Cohen, S. & Bethlehem, R. A. I. Synaptic and transcriptionally downregulated genes are associated with cortical thickness differences in autism. *Mol. Psychiatry* (2018). doi:10.1038/s41380-018-0023-7
5. Grothe, M. J. *et al.* Molecular properties underlying regional vulnerability to Alzheimer's disease pathology. *Brain* **141**, 2755–2771 (2018).
6. Morgan, S. E., Seidlitz, J., Whitaker, K. & Romero-Garcia, R. Cortical patterning of abnormal morphometric similarity in psychosis is associated with brain expression of schizophrenia related genes. *bioRxiv* (2018).
7. McColgan, P. *et al.* Brain Regions Showing White Matter Loss in Huntington's Disease Are Enriched for Synaptic and Metabolic Genes. *Biological Psychiatry* **83**, 456–465 (2018).
8. Fernandes, D. J. *et al.* Spatial gene expression analysis of neuroanatomical differences in mouse models. *Neuroimage* **163**, 220–230 (2017).
9. Kumar, V. J. *et al.* Linking spatial gene expression patterns to sex-specific brain structural changes on a mouse model of 16p11.2 hemideletion. *Transl. Psychiatry* **8**, 109 (2018).
10. Seidlitz, J. *et al.* Morphometric Similarity Networks Detect Microscale Cortical Organization and Predict Inter-Individual Cognitive Variation. *Neuron* **97**, 231–247.e7 (2018).
11. Hawrylycz, M. J. *et al.* An anatomically comprehensive atlas of the adult human brain transcriptome. *Nature* **489**, 391–399 (2012).

bioRxiv preprint doi: https://doi.org/10.1101/573279; this version posted March 16, 2019. The copyright holder for this preprint (which was not certified by peer review) is the author/funder, who has granted bioRxiv a license to display the preprint in perpetuity. It is made available under aCC-BY-NC-ND 4.0 International license.

12. Whitaker, K. J. *et al.* Adolescence is associated with genomically patterned consolidation of the hubs of the human brain connectome. *Proc. Natl. Acad. Sci. U. S. A.* **113**, 9105–9110 (2016).

13. Vértes, P. E. *et al.* Gene transcription profiles associated with inter-modular hubs and connection distance in human functional magnetic resonance imaging networks. *Philos. Trans. R. Soc. Lond. B Biol. Sci.* **371**, (2016).

14. Zhu, Y. *et al.* Spatiotemporal transcriptomic divergence across human and macaque brain development. *Science* **362**, (2018).

15. Tibshirani, R., Walther, G. & Hastie, T. Estimating the number of clusters in a data set via the gap statistic. *J. R. Stat. Soc. Series B Stat. Methodol.* **63**, 411–423 (2001).

16. Reardon, P. K. *et al.* Normative brain size variation and brain shape diversity in humans. *Science* **360**, 1222–1227 (2018).

17. Hill, J. *et al.* Similar patterns of cortical expansion during human development and evolution. *Proc. Natl. Acad. Sci. U. S. A.* **107**, 13135–13140 (2010).

18. Wagstyl, K. *et al.* Mapping Cortical Laminar Structure in the 3D BigBrain. *Cereb. Cortex* **28**, 2551–2562 (2018).

19. Paoloni-Giacobino, A., Chen, H. & Antonarakis, S. E. Cloning of a novel human neural cell adhesion molecule gene (NCAM2) that maps to chromosome region 21q21 and is potentially involved in Down syndrome. *Genomics* **43**, 43–51 (1997).

20. Sheng, L., Leshchyns'ka, I. & Sytnyk, V. Neural Cell Adhesion Molecule 2 (NCAM2)-Induced c-Src-Dependent Propagation of Submembrane Ca2+ Spikes Along Dendrites Inhibits Synapse Maturation. *Cereb. Cortex* (2018). doi:10.1093/cercor/bhy041

21. Raznahan, A. *et al.* Sex-chromosome dosage effects on gene expression in humans. *Proc. Natl. Acad. Sci. U. S. A.* **115**, 7398–7403 (2018).

22. Olmos-Serrano, J. L. *et al.* Down Syndrome Developmental Brain Transcriptome Reveals Defective Oligodendrocyte Differentiation and Myelination. *Neuron* **89**, 1208–1222 (2016).

bioRxiv preprint doi: https://doi.org/10.1101/573279; this version posted March 16, 2019. The copyright holder for this preprint (which was not certified by peer review) is the author/funder, who has granted bioRxiv a license to display the preprint in perpetuity. It is made available under aCC-BY-NC-ND 4.0 International license.

23. Prandini, P. *et al.* Natural gene-expression variation in Down syndrome modulates the outcome of gene-dosage imbalance. *Am. J. Hum. Genet.* **81**, 252–263 (2007).

24. Makarevitch, I. & Harris, C. Aneuploidy causes tissue-specific qualitative changes in global gene expression patterns in maize. *Plant Physiol.* **152**, 927–938 (2010).

25. Mankiw, C. *et al.* Allometric Analysis Detects Brain Size-Independent Effects of Sex and Sex Chromosome Complement on Human Cerebellar Organization. *J. Neurosci.* **37**, 5221–5231 (2017).

26. Fish, A. M. *et al.* Influences of Brain Size, Sex, and Sex Chromosome Complement on the Architecture of Human Cortical Folding. *Cereb. Cortex* **27**, 5557–5567 (2017).

27. Reardon, P. K. *et al.* An Allometric Analysis of Sex and Sex Chromosome Dosage Effects on Subcortical Anatomy in Humans. *J. Neurosci.* **36**, 2438–2448 (2016).

28. Giedd, J. N. *et al.* Child psychiatry branch of the National Institute of Mental Health longitudinal structural magnetic resonance imaging study of human brain development. *Neuropsychopharmacology* **40**, 43–49 (2015).

29. Elliott, C. D. Differential ability scales--second edition: Administration and scoring manual. (2007).

30. Kaufman, A. S. *Kaufman Brief Intelligence Test: KBIT 2 ; Manual*. (Pearson, 2004).

31. Cutter, W. J. *et al.* Influence of X chromosome and hormones on human brain development: a magnetic resonance imaging and proton magnetic resonance spectroscopy study of Turner syndrome. *Biol. Psychiatry* **59**, 273–283 (2006).

32. Raznahan, A. *et al.* Cortical anatomy in human X monosomy. *Neuroimage* **49**, 2915–2923 (2010).

33. van Amelsvoort, T. *et al.* Brain Anatomy in Adults With Velocardiofacial Syndrome With and Without Schizophrenia: Preliminary Results of a Structural Magnetic Resonance Imaging Study. *Arch. Gen. Psychiatry* **61**, 1085–1096 (2004).

34. Campbell, L. E. *et al.* Brain and behaviour in children with 22q11.2 deletion syndrome: a

bioRxiv preprint doi: https://doi.org/10.1101/573279; this version posted March 16, 2019. The copyright holder for this preprint (which was not certified by peer review) is the author/funder, who has granted bioRxiv a license to display the preprint in perpetuity. It is made available under aCC-BY-NC-ND 4.0 International license.

volumetric and voxel-based morphometry MRI study. *Brain* **129**, 1218–1228 (2006).

35. Canavan, A. G. M., Dunn, G. & McMillan, T. M. Principal components of the WAIS-R. *British Journal of Clinical Psychology* **25**, 81–85 (1986).
36. Ad-Dab'bagh, Y. *et al.* The CIVET image-processing environment: a fully automated comprehensive pipeline for anatomical neuroimaging research. in *Proceedings of the 12th annual meeting of the organization for human brain mapping* 2266 (Florence, Italy, 2006).
37. Harwell, J., Van Essen, D., Hanlon, D. & Dickson, J. Integrated software for surface-based analyses of cerebral cortex. *Neuroimage* **13**, 148 (2001).
38. Romero-Garcia, R., Atienza, M., Clemmensen, L. H. & Cantero, J. L. Effects of network resolution on topological properties of human neocortex. *Neuroimage* **59**, 3522–3532 (2012).
39. Desikan, R. S. *et al.* An automated labeling system for subdividing the human cerebral cortex on MRI scans into gyral based regions of interest. *Neuroimage* **31**, 968–980 (2006).
40. Romero-Garcia, R. *et al.* Structural covariance networks are coupled to expression of genes enriched in supragranular layers of the human cortex. *Neuroimage* **171**, 256–267 (2018).
41. Váša, F. *et al.* Adolescent Tuning of Association Cortex in Human Structural Brain Networks. *Cereb. Cortex* **28**, 281–294 (2018).
42. Richiardi, J. *et al.* BRAIN NETWORKS. Correlated gene expression supports synchronous activity in brain networks. *Science* **348**, 1241–1244 (2015).
43. Guna, A., Butcher, N. J. & Bassett, A. S. Comparative mapping of the 22q11.2 deletion region and the potential of simple model organisms. *J. Neurodev. Disord.* **7**, 18 (2015).
44. Fischl, B. FreeSurfer. *Neuroimage* **62**, 774–781 (2012).
45. de Jong, S. SIMPLS: An alternative approach to partial least squares regression. *Chemometrics Intellig. Lab. Syst.* **18**, 251–263 (1993).
46. Ergon, R. Principal component regression (PCR) and partial least squares regression

bioRxiv preprint doi: https://doi.org/10.1101/573279; this version posted March 16, 2019. The copyright holder for this preprint (which was not certified by peer review) is the author/funder, who has granted bioRxiv a license to display the preprint in perpetuity. It is made available under aCC-BY-NC-ND 4.0 International license.

(PLSR). *Mathematical and Statistical Methods in Food Science and Technology* 121–142 (2013). doi:10.1002/9781118434635.ch8

47. Eden, E., Navon, R., Steinfeld, I., Lipson, D. & Yakhini, Z. GOrilla: a tool for discovery and visualization of enriched GO terms in ranked gene lists. *BMC Bioinformatics* **10**, 48 (2009).
48. Eden, E., Lipson, D., Yogev, S. & Yakhini, Z. Discovering motifs in ranked lists of DNA sequences. *PLoS Comput. Biol.* **3**, e39 (2007).
49. Zhang, Y. *et al.* Purification and Characterization of Progenitor and Mature Human Astrocytes Reveals Transcriptional and Functional Differences with Mouse. *Neuron* **89**, 37–53 (2016).
50. Lake, B. B. *et al.* Integrative single-cell analysis of transcriptional and epigenetic states in the human adult brain. *Nat. Biotechnol.* **36**, 70–80 (2018).
51. Habib, N. *et al.* Massively parallel single-nucleus RNA-seq with DroNc-seq. *Nat. Methods* **14**, 955–958 (2017).
52. Darmanis, S. *et al.* A survey of human brain transcriptome diversity at the single cell level. *Proc. Natl. Acad. Sci. U. S. A.* **112**, 7285–7290 (2015).
53. Li, M. *et al.* Integrative functional genomic analysis of human brain development and neuropsychiatric risks. *Science* **362**, (2018).
54. McKenzie, A. T. *et al.* Brain Cell Type Specific Gene Expression and Co-expression Network Architectures. *Sci. Rep.* **8**, 8868 (2018).
55. Amunts, K. *et al.* BigBrain: an ultrahigh-resolution 3D human brain model. *Science* **340**, 1472–1475 (2013).
56. Paquola, C. *et al.* Dissociations between microstructural and functional hierarchies within regions of transmodal cortex. *bioRxiv* 488700 (2018). doi:10.1101/488700

bioRxiv preprint doi: https://doi.org/10.1101/573279; this version posted March 16, 2019. The copyright holder for this preprint (which was not certified by peer review) is the author/funder, who has granted bioRxiv a license to display the preprint in perpetuity. It is made available under aCC-BY-NC-ND 4.0 International license.

Acknowledgments

The authors would like to thank the patients and their families for their participation in this study. The authors also thank Francis McMahon and members of the Human Genetics Branch for helpful discussions. This work was supported by the Intramural Research Program of the National Institute of Mental Health and the *Eunice Kennedy Shriver* National Institute of Child Health (Clinical Protocol no. 89-M-006 and 08-CH-213; Clinical trial reg. no. NCT00001246 and NCT00758108 clinicaltrials.gov; NIH Annual Report Number, ZIA MH002794-13 and NICHD 1-ZIA-HD008898). JS was supported by the NIH Oxford-Cambridge Scholars' Program. FV was supported by the Gates Cambridge Trust. RAIB was supported by a Postdoctoral Fellowship from the British Academy. PEV was supported by the Medical Research Council (MR/K020706/1) and by MQ: Transforming Mental Health (MQF17_24). She is a Fellow of the Alan Turing Institute funded under the EPSRC grant EP/N510129/1. SEM was supported by a Henslow Fellowship at Lucy Cavendish College, University of Cambridge, funded by the Cambridge Philosophical Society. JCH was supported by an NIH Bench-to-Bedside grant.

Author Contributions

JS, ETB, and AR conceived of the project. JS performed the analyses. FML, LSC, JB, JCH, NRL, DGM, and AR were involved in data collection. AN, SL, RAIB, PEV, SEM, RR-G, FV, CP, BB, KW, DP, LdlT-U, and DHG provided critical input on the methods and analyses. ETB and AR supervised the project. JS, ETB, and AR wrote the initial manuscript. All authors edited and contributed to the final version of the manuscript.

Author Information

ETB is employed half-time by the University of Cambridge and half-time by GlaxoSmithKline; he holds stock in GlaxoSmithKline.

bioRxiv preprint doi: https://doi.org/10.1101/573279; this version posted March 16, 2019. The copyright holder for this preprint (which was not certified by peer review) is the author/funder, who has granted bioRxiv a license to display the preprint in perpetuity. It is made available under aCC-BY-NC-ND 4.0 International license.

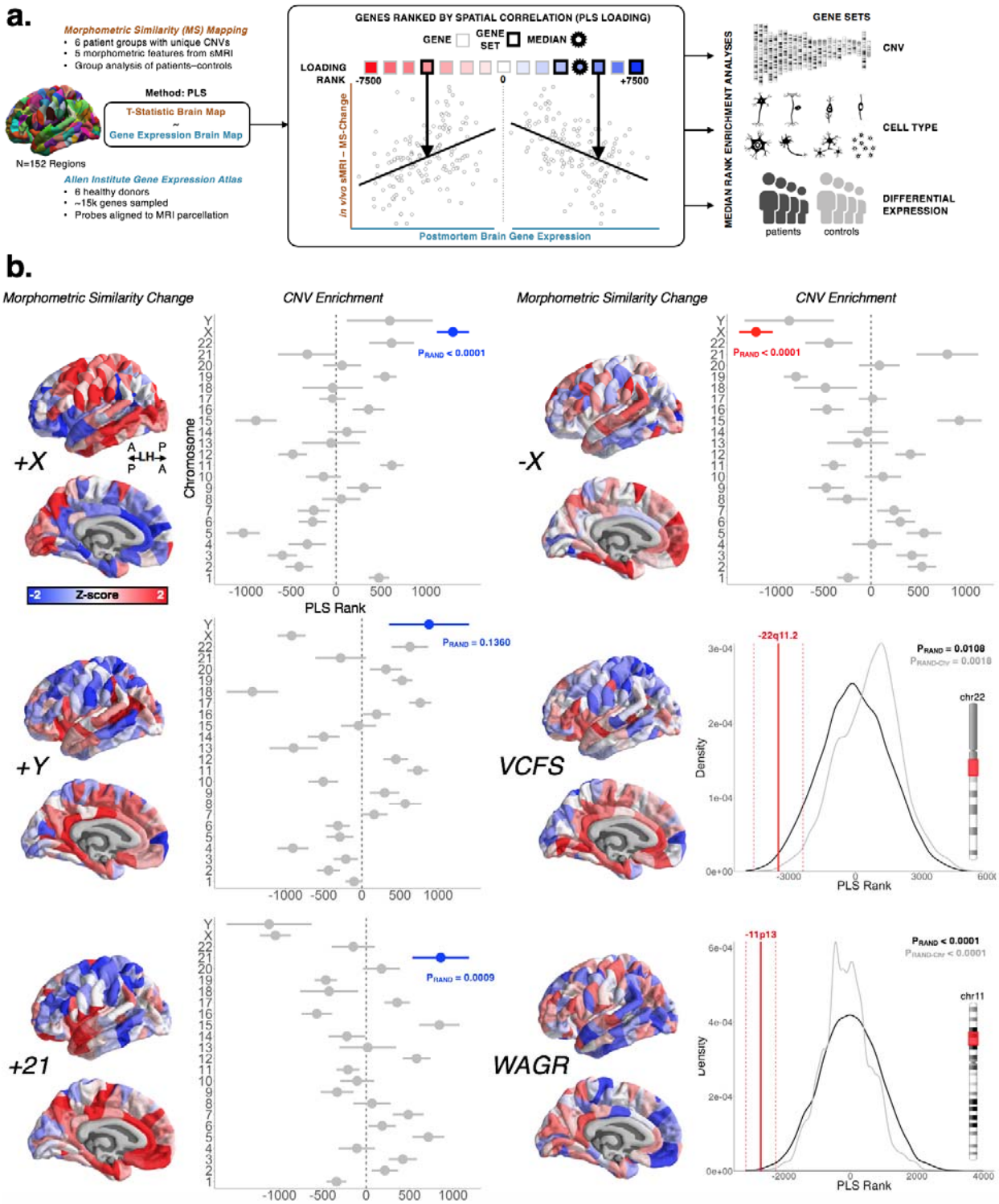

Fig. 1. Transcriptomic specificity of neuroanatomical effects. a) Schematic outlining the main imaging-transcriptomic enrichment analyses and statistical tests. **b)** (left) Surface projections of T-statistics (z-scored for plotting purposes) for CNV effects on regional morphometric similarity (MS). Despite some overlap across CNVs, each CNV induces a distinct profile of MS change. For full chromosome CNVs, neighboring pointrange plots show the

bioRxiv preprint doi: https://doi.org/10.1101/573279; this version posted March 16, 2019. The copyright holder for this preprint (which was not certified by peer review) is the author/funder, who has granted bioRxiv a license to display the preprint in perpetuity. It is made available under aCC-BY-NC-ND 4.0 International license.

median (point) and standard error (range) rank of each chromosomal gene set - based on gene rankings from the PLS analysis (see Fig. 1a). The chromosomal gene set for each CNV possessed a more extreme median rank than all other chromosomal gene sets, and the polarity of this effect was opposite for chromosomal duplications (CNV gene set high ranked) vs. deletion (CNV gene set low ranked). For sub-chromosomal CNVs (depicted as red in the respective chromosome ideograms), density plots show median (solid line) and standard error (dashed line) ranks for the relevant CNV gene set. Observed ranks are shown relative to two null distributions: P_{RAND} (black), and $P_{RAND\text{-}Chr}$ (gray). P_{RAND} was calculated using 10000 gene rank permutations (black). $P_{RAND\text{-}Chr}$ was calculated similarly to P_{RAND} but only sampling gene ranks from the respective chromosome of the CNV.

bioRxiv preprint doi: https://doi.org/10.1101/573279; this version posted March 16, 2019. The copyright holder for this preprint (which was not certified by peer review) is the author/funder, who has granted bioRxiv a license to display the preprint in perpetuity. It is made available under aCC-BY-NC-ND 4.0 International license.

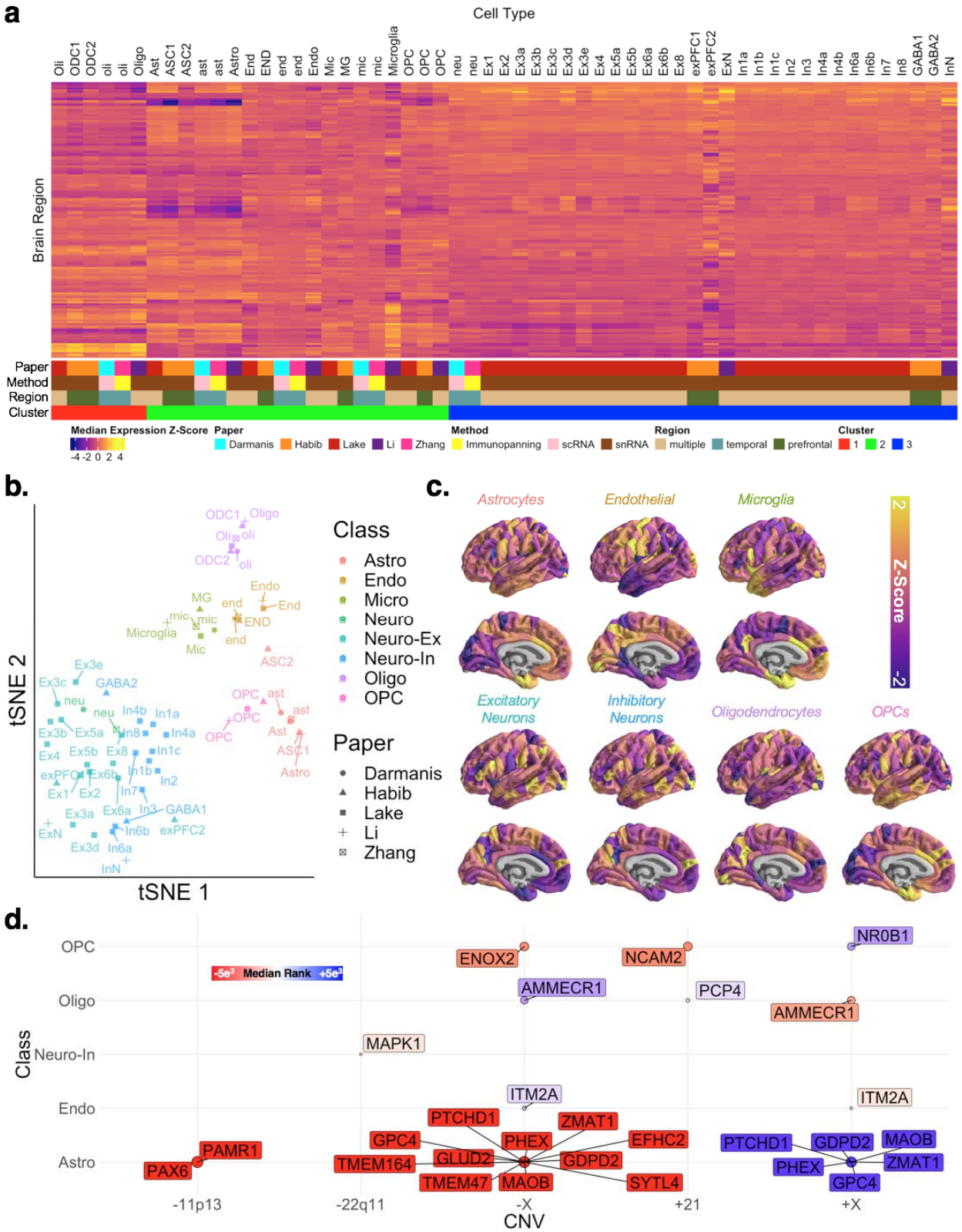

Fig. 2. Cell type decoding of AHBA microarray and CNV gene ranks. a) Regional median expression (Z-score) in the AIBS microarray dataset of cell-specific gene sets, aggregated across 5 single-cell sequencing studies and ordered according to hierarchical clustering (n=3

bioRxiv preprint doi: https://doi.org/10.1101/573279; this version posted March 16, 2019. The copyright holder for this preprint (which was not certified by peer review) is the author/funder, who has granted bioRxiv a license to display the preprint in perpetuity. It is made available under aCC-BY-NC-ND 4.0 International license.

clusters based on gap statistic). Cell type abbreviations are maintained from the original study (see also Extended Data File 3). **b)** T-distributed stochastic neighborhood embedding (tSNE) of cell-specific gene sets based on their spatial expression profiles distinguishes 7 canonical cell classes (color coded). **c)** Regional weighted expression maps (see Methods) of each canonical cell class from Fig. 2b. **d)** Significant associations between cell classes and MS change in different CNVs. Circles indicate cell classes with gene sets that show statistically median rank enrichment relative to PLS-derived ranked gene lists for each CNV disorder ($P_{RAND} < 0.05$). Circles color indicates the direction of median rank enrichment: red circled cell classes show high expression in brain regions where MS is greater in patients that controls (vice versa for blue circles). Named genes for each cell class are (i) expressed by the cell, (ii) in the respective CNV, and (iii) highly correlated with regional variation in MS change for that CNV (i.e. in the top 5% of PLS ranks).

bioRxiv preprint doi: https://doi.org/10.1101/573279; this version posted March 16, 2019. The copyright holder for this preprint (which was not certified by peer review) is the author/funder, who has granted bioRxiv a license to display the preprint in perpetuity. It is made available under aCC-BY-NC-ND 4.0 International license.

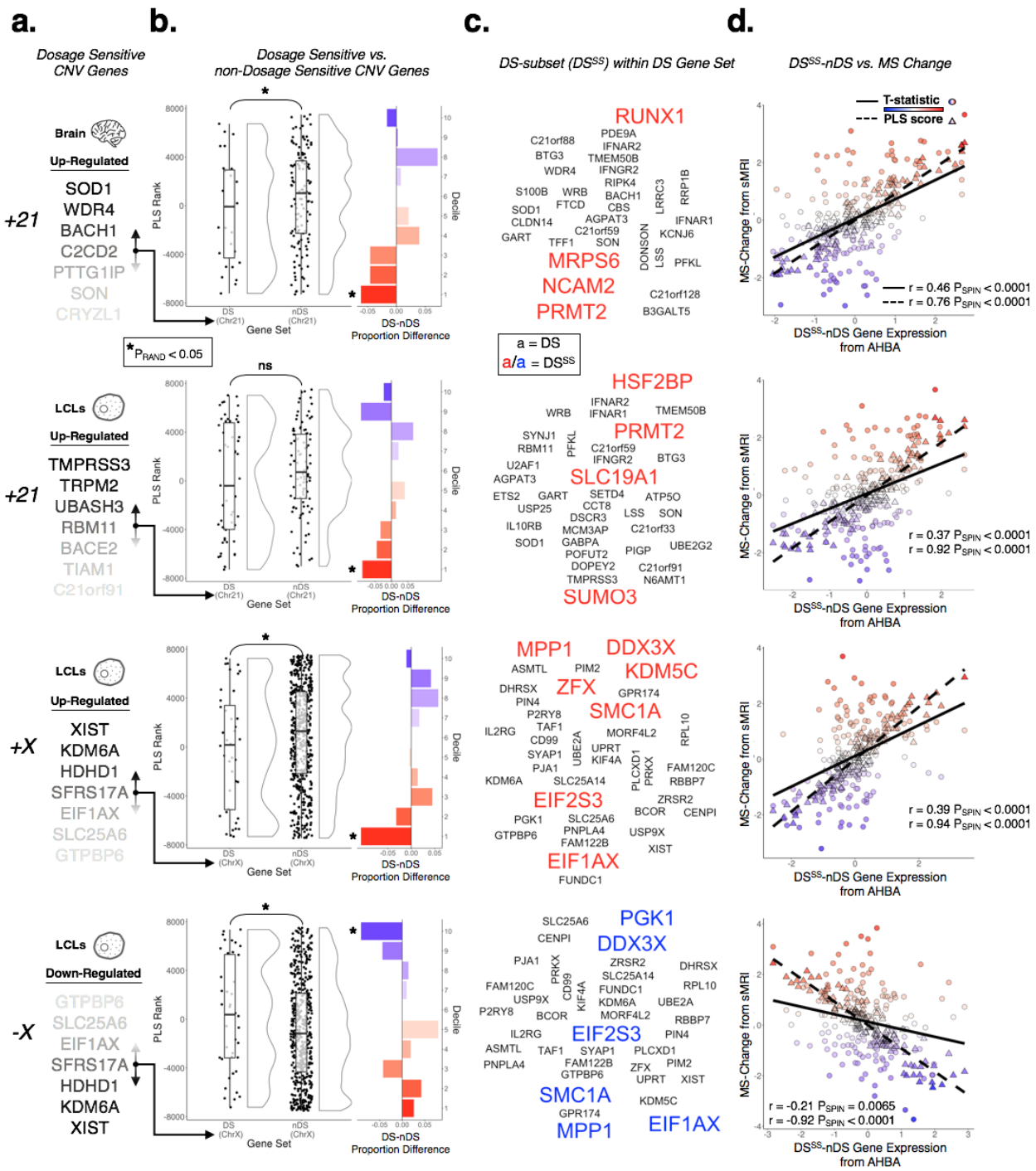

Fig. 3. CNV gene dosage sensitivity predicts spatial coupling between gene expression and anatomical change. a) Top dosage sensitive (DS) genes in brain tissue and blood-derived lymphoblastoid cell lines (LCLs) from CNV carriers (brain: +21. LCLs: +21,+X,-X, Methods). **b)** Raincloud plots showing the different distributions of ranks for DS and non-DS (nDS) genes. Boxplots show the median and interquartile ranges. Neighboring barplots show decile-specific differences in proportions of DS vs. nDS genes. The statistically significant (P_{RAND} < 0.05) median rank differences between DS and nDS gene sets are driven by a subset of DS genes (DS^{SS}), which are significantly enriched at extreme ranks. **c)** DS^{SS} gene names highlighted from

bioRxiv preprint doi: https://doi.org/10.1101/573279; this version posted March 16, 2019. The copyright holder for this preprint (which was not certified by peer review) is the author/funder, who has granted bioRxiv a license to display the preprint in perpetuity. It is made available under aCC-BY-NC-ND 4.0 International license.

the DS gene set. **d)** Spatial correlations between DS^{SS}-nDS differential gene expression and both regional PLS scores and regional MS change for each CNV.

bioRxiv preprint doi: https://doi.org/10.1101/573279; this version posted March 16, 2019. The copyright holder for this preprint (which was not certified by peer review) is the author/funder, who has granted bioRxiv a license to display the preprint in perpetuity. It is made available under aCC-BY-NC-ND 4.0 International license.

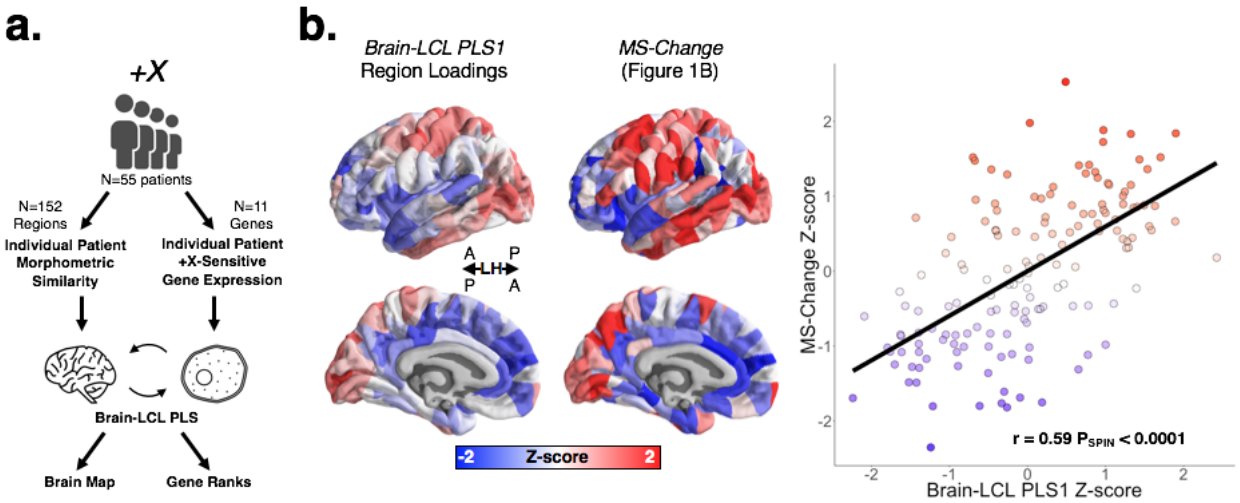

Fig. 4. Severity of altered gene expression predicts severity of regional anatomical change across patients. a) Schematic outlining analytic approach to interrelating cortical MS changes from MRI and DS gene expression from LCLs in +X patients. **b)** (left) Regional loadings for principal component of shared variance between MS change in brain and DS gene expression in LCLs. (middle) Regional MS change in +X patients compared to controls (from Fig. 1a). Spatial similarity between these maps indicates that +X patients with greater dysregulation of DS genes in blood show a more pronounced manifestation of the +X MS change map. (right) This spatial similarity is quantitatively strong (r=0.59) and statistically significant (P_{SPIN}<0.0001)

bioRxiv preprint doi: https://doi.org/10.1101/573279; this version posted March 16, 2019. The copyright holder for this preprint (which was not certified by peer review) is the author/funder, who has granted bioRxiv a license to display the preprint in perpetuity. It is made available under aCC-BY-NC-ND 4.0 International license.

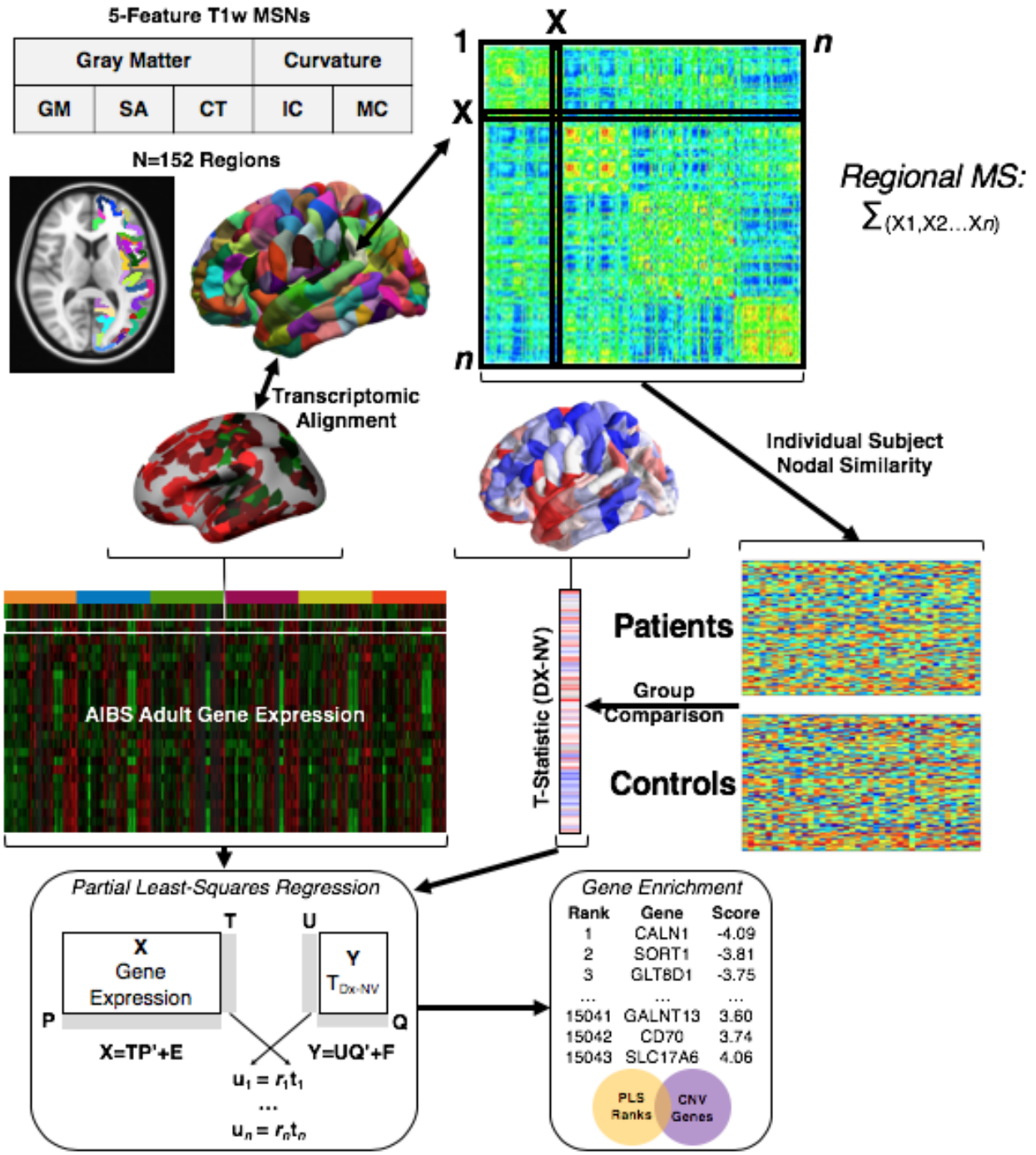

Fig. S1. Schematic overview of methodological pipeline. Morphometric Similarity Networks (MSNs) are constructed for each subject with 5 cortical features derived from structural (T1-weighted) MRI. Regional morphometric similarity (MS) is calculated as the average of unthresholded edges (correlations). Linear regression yields T-statistics for CNV effects (patients vs. controls) on each region's MS estimates. Partial least squares (PLS) regression is performed to generate a ranked list of genes with correlations between regional gene expression and regional MS T-statistics (Methods).

bioRxiv preprint doi: https://doi.org/10.1101/573279; this version posted March 16, 2019. The copyright holder for this preprint (which was not certified by peer review) is the author/funder, who has granted bioRxiv a license to display the preprint in perpetuity. It is made available under aCC-BY-NC-ND 4.0 International license.

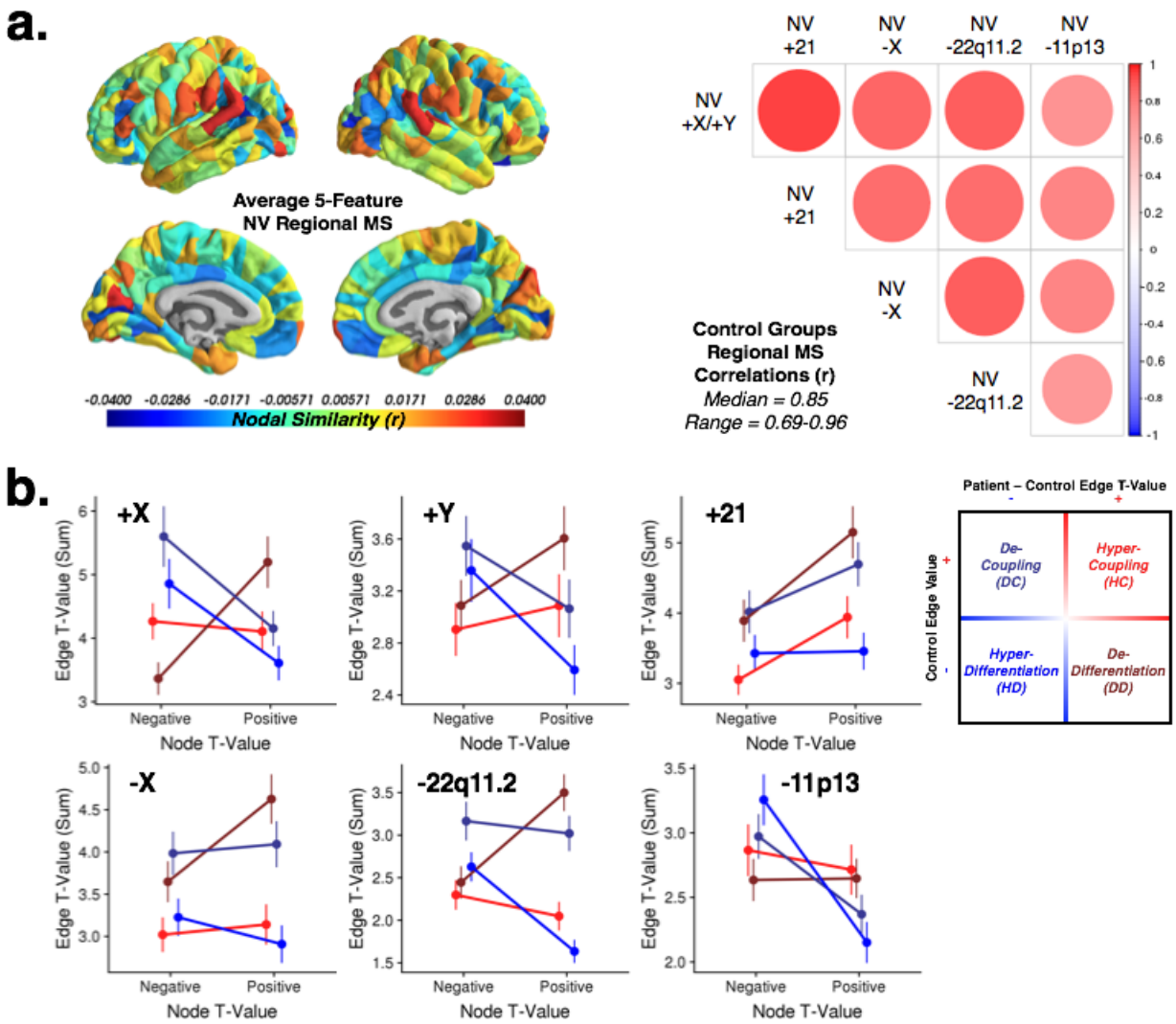

Fig. S2. Consistency and interpretation of neuroanatomical effects. a) (Left) Average regional morphometric similarity (MS) across all 4 independent cohorts of typically-developing controls. There was relatively high regional MS in temporal and parietal regions, and relatively low regional MS in ventromedial prefrontal regions. (Right) Correlation in average regional MS between each set of controls. There was significantly high positive correspondence between the topographies of regional MS (median Pearson's r = 0.85). **b)** Interpretation of patient-control MS change. Plots show the sum of the absolute T-statistics of CNV effects on MS edges within the four possible classes of effects (y-axis), for the top 10 most positive and negative regional T-statistics (x-axis). The key shows the four possible outcomes. For each CNV, the regional T-statistics observed (Fig. 1b) arise from a unique combination of the four effects at the edge level. In general, negative regional T-statistics tend to reflect morphometric decoupling in CNV patients relative to controls, whereas positive regional values tend to reflect morphometric de-differentiation in CNV patients relative to controls (see Methods). NV = normal volunteers.

bioRxiv preprint doi: https://doi.org/10.1101/573279; this version posted March 16, 2019. The copyright holder for this preprint (which was not certified by peer review) is the author/funder, who has granted bioRxiv a license to display the preprint in perpetuity. It is made available under aCC-BY-NC-ND 4.0 International license.

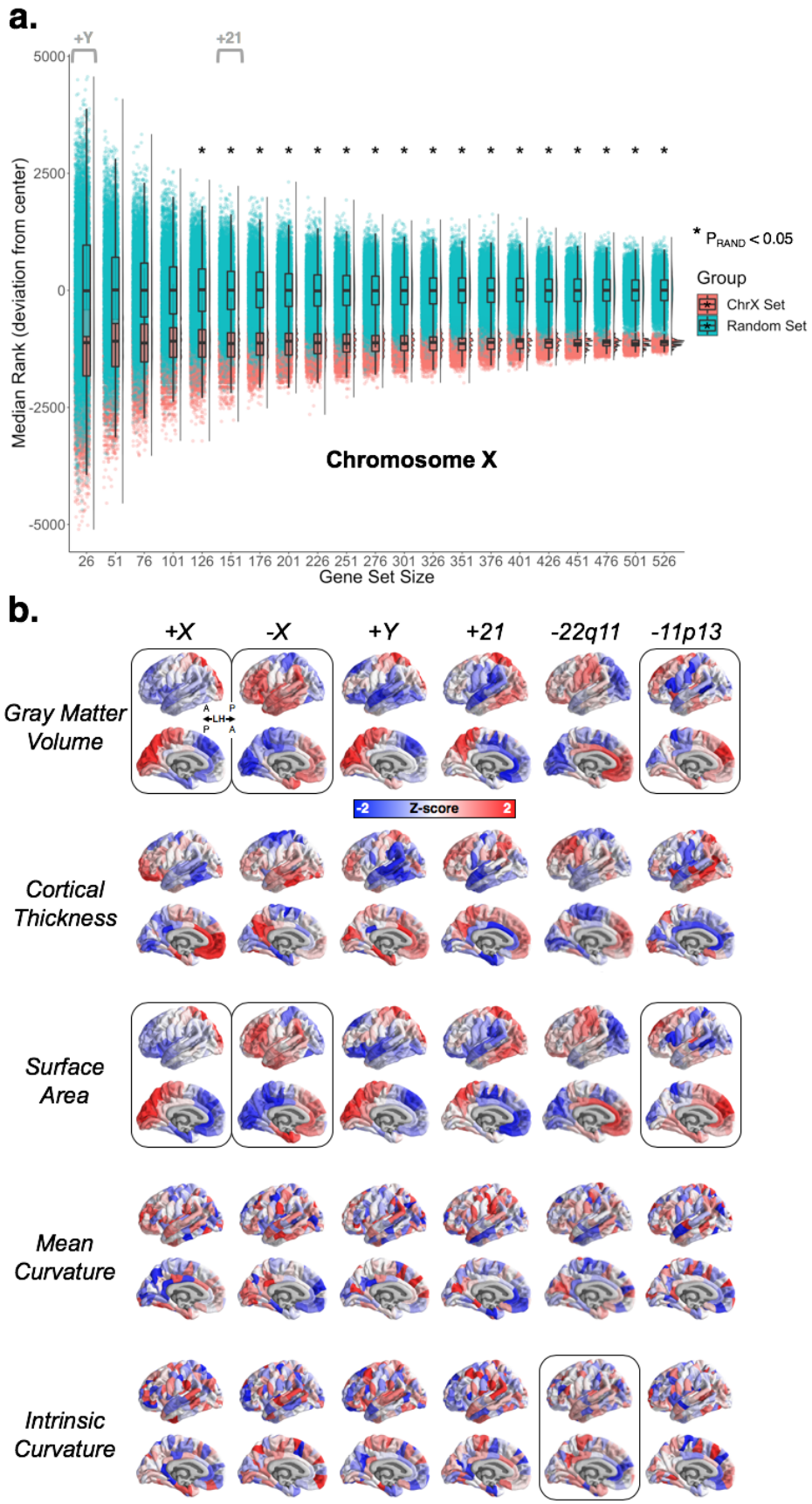

bioRxiv preprint doi: https://doi.org/10.1101/573279; this version posted March 16, 2019. The copyright holder for this preprint (which was not certified by peer review) is the author/funder, who has granted bioRxiv a license to display the preprint in perpetuity. It is made available under aCC-BY-NC-ND 4.0 International license.

Fig. S3. Gene set size and constituent features of neuroanatomical effects. a) Raincloud plot demonstrating consistency of effect-size between size-varying subsamples of X-chromosome gene ranks for the +X CNV (blue), and random gene subsamples of similar size (red). Boxplots show the median and interquartile ranges. Median ranks are highly consistent, but variation in gene rank increases with reducing gene set size. Black asterisks denote significance of median differences, with a ~100 genes being the smallest gene set size necessary to consistently reach significance at $P_{RAND} = 0.05$. Gray annotations denote the +Y and +21 CNVs, showing that they fall within the expected trend for significance based on gene sets of similar size within the X-chromosome. **b)** Regional T-statistics (CNV patients vs. controls) computed using individual constituent features of the morphometric similarity networks. The CNV gene set ranks linked to these alternative anatomical change maps are provided in Table S3. Black outlines denote anatomical change maps which successfully recover the preferential spatial coupling between anatomical change and expression of CNV region genes in the human cortex ($P_{RAND} < 0.05$).

bioRxiv preprint doi: https://doi.org/10.1101/573279; this version posted March 16, 2019. The copyright holder for this preprint (which was not certified by peer review) is the author/funder, who has granted bioRxiv a license to display the preprint in perpetuity. It is made available under aCC-BY-NC-ND 4.0 International license.

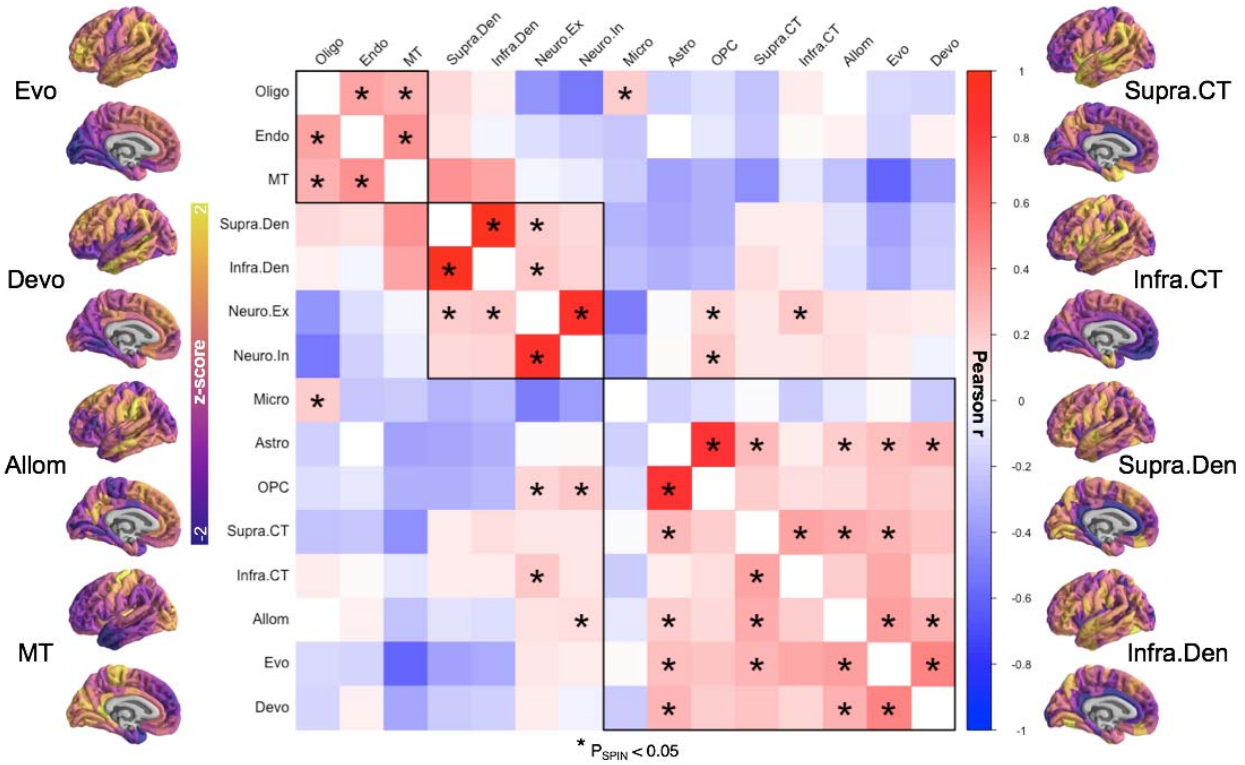

Fig. S4. Correlations between cell class expression and canonical in vivo and ex vivo maps of cortical microstructure. Pairwise Pearson correlation coefficients (across cortical regions) are plotted for all map pairs. Asterisks denote correlations with $P_{SPIN} < 0.05$. The comparison maps are plotted with the same color scale as the cell class maps in Fig. 2B. From in vivo: Evo = evolutionary scaling; Devo = developmental scaling; Allom = allometric scaling; MT = magnetization transfer; From ex vivo (BigBrain): Supra.CT = supragranular cortical thickness; Infra.CT = infragranular cortical thickness; Supra.Den = supragranular density; Infra.Den = infragranular density. Details and references for these maps can be found in the Methods.

bioRxiv preprint doi: https://doi.org/10.1101/573279; this version posted March 16, 2019. The copyright holder for this preprint (which was not certified by peer review) is the author/funder, who has granted bioRxiv a license to display the preprint in perpetuity. It is made available under aCC-BY-NC-ND 4.0 International license.

Table S1.
Demographic Information

CNV	*Syndrome*	*Site**	*Number of Subjects* *Patients* *Controls*	*Age (mean, SD)* *Patients* *Controls*
XXX, XXY, XXYY (+X)	X aneuploidy	NIH	106 (20 XXYY) 165 (79 Females)	12.93, 5.22 12.82, 4.83
XYY, XXYY (+Y)	Y aneuploidy	NIH	46 (20 XXYY) 165 (79 Females)	13.17, 5.16 12.82, 4.83
Trisomy 21 (+21)	Down Syndrome	NIH	26 (13 Females) 42 (21 Females)	15.52, 5.67 15.46, 5.76
XO (-X)	Turner Syndrome (X aneuploidy)	IoP	20 Females 36 (All Females)	24, 8.78 39, 20.26
22q11.2 Deletion	Velocardiofacial Syndrome	IoP	29 (13 Females) 27 (11 Females)	12.10, 3.06 11.52, 2.36
11p13 Deletion	WAGR Syndrome	NIH	24 (10 Females) 17 (8 Females)	13.45, 6.70 16.03, 7.03

* NIH = National Institutes of Health (USA); IoP = Institute of Psychiatry (UK)